DEPARTMENT OF PHYSICS
UNIVERSITY OF JYVÄSKYLÄ
RESEARCH REPORT No. 8/2004

ULTRASONIC GUIDED WAVE MEASUREMENTS IN BONE

BY
PETRO MOILANEN

Academic Dissertation
for the Degree of
Doctor of Philosophy

To be presented, by permission of the
Faculty of Mathematics and Natural Sciences
of the University of Jyväskylä,
for public examination in Auditorium FYS-1 of the
University of Jyväskylä on December 17, 2004
at 12 o'clock noon

Jyväskylä, Finland
December 2004

ISBN 978-951-39-3157-5
URN:ISBN:978-951-39-3157-5

Author's address:
Petro Moilanen
Department of Health Sciences
P.O. BOX 35 (LL)
40014 University of Jyväskylä
Finland
Tel. +358 14 260 2188
pemoilan@cc.jyu.fi

Supervisors:
Professor Jussi Timonen, Ph.D.
Department of Physics
University of Jyväskylä

Professor Sulin Cheng, Ph.D.
Department of Health Sciences
University of Jyväskylä

Senior Researcher Patrick H.F. Nicholson, Ph.D.
Department of Health Sciences
University of Jyväskylä

Reviewers:
Professor Jukka S. Jurvelin, Ph.D.
Department of Applied Physics
University of Kuopio
Finland

Associate Professor Robin Cleveland, Ph.D.
Department of Aerospace and Mechanical Engineering
University of Boston
United States of America

Opponent:
Dr. Christian M. Langton, Ph.D.
Centre for Metabolic Bone Disease
Hull Royal Infirmary
United Kingdom

ISBN: 951-39-1986-2
ISSN: 0075-465X

Abstract

Osteoporosis is a widespread and growing clinical problem, and provides the primary motivation for developing improved methods for the in vivo assessment of bone. Such methods should ideally be easy to use, safe, inexpensive, reliable, and, above all, should provide clinically-useful information. They should be sensitive to the early signs of bone deterioration, so that problems can be detected early and the benefits of treatment can be maximised. As the existing diagnostic methods, based mainly on X-ray absorption, can only provide information on bone density and geometry, there is growing interest in ultrasonic methods which have the potential to assess aspects of the material properties of bone.

The aim of the present study was to evaluate the feasibility of using ultrasonic guided waves for the quantitative assessment of bone. A prototype device was developed for low frequency ultrasonic transmission measurements along human long bones. Analytical plate and tube models were used for identification of the measured wave modes. The phase velocities of two guided wave modes were thereby determined. In addition, an inversion scheme was developed for determining the cortical bone thickness from guided wave ultrasound data.

Experimental work confirmed that guided waves could be excited and detected in human bones as well as in bone phantoms. Data from a small scale clinical pilot study indicated increased sensitivity to osteoporosis for guided wave measurements. A large scale in vivo study in a group of 106 pubertal girls was completed, and this demonstrated that guided wave measurements were sensitive to both bone material properties and bone thickness. A comparative in vitro study for human radius specimens indicated that the velocity of the fundamental antisymmetric guided wave correlated significantly with cortical bone mineral density, as did the lateral wave velocities measured with other devices. However, this guided wave velocity had an advantage over any lateral wave measurement in that it was significantly correlated with cortical bone thickness as well as mineral density. In addition, it was demonstrated that the use of an inversion scheme, based on plate or tube theory, enables respectively the assessment of plate or tube wall thickness. It was shown also, that the use of tube model is preferred when analysing guided wave measurements for thick-walled bones.

Despite the successes listed above, problems have been identified that must be addressed before guided wave measurements can progress as a reliable and useful clinical technique. In the work to date the effects of the soft tissue overlying the bone have been found to be a major factor. It is proposed that the key issue in understanding this problem is to consider wave propagation in a bilayer system, composed of solid bone and liquid-like soft tissue. The initial results in immersed bone phantoms suggest that the use of an adequate bilayer theory can potentially eliminate the influence of soft tissue on the in vivo guided wave measurements. The results for human bones in vivo are under way of being analysed.

Based on these results, it is concluded that the measurement of ultrasonic guided waves in human long bones is indeed feasible and offers advantages over existing techniques. However, further modelling of guided waves is of crucial importance for a precise and reliable interpretation of clinical guided wave measurements in bone.

Preface

The work reviewed in this thesis has been carried out in the Departments of Health Sciences and Physics at the University of Jyväskylä from January 2001 to December 2004.

I would like to thank my supervisors, Prof. Jussi Timonen and Prof. Sulin Cheng for the opportunity to chase my skills in this challenging interdisciplinary project, in an international collaboration with leading scientists. You have encouraged me during the process and taught me to face problems with open mind. I would like to address my great gratitude to my instructor, Dr. Patrick Nicholson for inspiring ideas, encouragement and patience in teaching scientific work. Especially, I would like to thank Mr. Vantte Kilappa for conscientiously and carefully performing a great deal of experimental hard work. I would also like to thank Dr. Pascal Laugier for sharing bone samples, Dr. Maryline Talmant for invaluable help with guided wave modelling, Ms. Marie Muller for collaborating with a publication, Prof. Tommi Kärkkäinen for invaluable help with signal analysis routines, Dr. Erkki Heikkola for writing the programs for numerical modelling of wave propagation, and everyone in the CALEX group for invaluable help with the in vivo measurements. It has been great for working with all of you.

I would like to address my gratitude to the official reviewers, Prof. Jukka Jurvelin and Prof. Robin Cleveland, for critical and thorough reading of the manuscript.

The financial support from Jenny and Antti Wihuri Foundation, Tekes, JSP Facilities, and Foundation for Finnish Inventions is gratefully acknowledged.

My warmest thanks go to my loving wife, Miia. You have given me balance and motivation; you have had an extraordinary role in this work as also having been one of my colleagues at the first meters. Finally, I would like to thank my parents Iris and Lasse, sister Saija, step-mother Marja, and parents-in-law Eila and Osmo for your invaluable support.

Säynätsalo, December 2004

Petro Moilanen

Contents

List of publications

This thesis consists of an overview and the following publications:

- **I** P.H.F. Nicholson, P. Moilanen, T. Kärkkäinen, J. Timonen and S. Cheng, *Guided ultrasonic waves in long bones: modelling, experiment and in vivo application*, Physiol Meas **23** (2002) 755-768.
- **II** P. Moilanen, P.H.F. Nicholson, T. Kärkkäinen, Q. Wang, J. Timonen and S. Cheng, *Assessment of the tibia using ultrasonic guided waves in prepubertal girls*, Osteoporos Int **14** (2003) 1020-1027.
- **III** P. Moilanen, V. Kilappa, P.H.F. Nicholson, J. Timonen and S. Cheng, *Thickness sensitivity of ultrasound velocity in long bone phantoms*, Ultrasound in Med and Biol **30** (2004) 1517-1521.
- **IV** M. Muller, P. Moilanen, E. Bossy, V. Kilappa, P.H.F. Nicholson, J. Timonen, M. Talmant, S. Cheng and P. Laugier, *In vitro comparison of three different approaches using ultrasonic axial transmission for cortical bone assessment,* Submitted for publication.
- **V** P. Moilanen, P.H.F. Nicholson, V. Kilappa, J. Timonen and S. Cheng, *Measuring the phase velocity of guided waves in free and immersed plates as bone phantoms*, Submitted for publication.

The author has had an active role in all stages of the research. He has been involved in planning and conducting the research. He has assembled the ultrasound device and performed all the experimental measurements used in Publications I and II. He has designed and developed the methods of analysis for the ultrasonic guided wave measurements used in all five Publications. He has developed a numerical routine for determining the dispersion curves based on the analytical theory of guided waves, which have been used as the basis for Publications I, II, IV and V. He has actively contributed to the ideas reported in Publications I and IV, and written parts of them. He has written publication V and the first drafts of publications II and III.

Chapter 1

Introduction

Osteoporosis is a widespread and growing clinical problem which most often manifests itself clinically as fractures of the wrist, spine or hip. Therefore understanding the determinants of fracture risk is of crucial importance. The changes seen in osteoporotic bone include density changes (e.g. reduced trabecular and cortical bone mineral density), geometrical changes (e.g. reduced bone thickness and cross-sectional area) and mechanical changes (e.g. reduced strength and stiffness).

Diagnostic methods based on x-ray absorption are the current “gold standard” for quantitative assessment of bone but they provide incomplete information. Whilst they can provide reasonably good data for bone mineral density (BMD) and geometry, they are not intrinsically sensitive to the mechanical properties or microarchitecture of bone. The clinical value of such additional information has yet to be conclusively demonstrated, but there is growing interest in the potential for assessing aspects of bone “quality” in addition to “quantity”. In addition, X-ray technologies are expensive, non-portable and use ionizing radiation with a consequent health risk. Ultrasound offers an alternative approach to bone assessment that has a unique potential to characterise the material and structural properties of bone. Furthermore, ultrasound is safe, relatively cheap, and portable.

The ultrasonic methods and devices can be divided into two main categories according to the type of bone (trabecular or cortical, see Chapter 2) to be measured. More attention has been paid to measuring the trabecular bone, at sites such as the heel [35, 28, 23] or finger phalanges [75, 91]. These methods are generally seen as being more directly relevant to the sites (hip and spine) where osteoporotic fractures most often occur. It must be noted, that direct ultrasonic measurement of the hip and spine is difficult as these sites are located deep under soft tissue. It has been shown, however, that ultrasound attenuation (referred to as Broadband Ultrasound Attenuation, BUA) or speed of sound (SOS), as measured for the heel, predict fractures at hip [35, 9, 82, 28, 45] and spine [38, 23]. In addition, the interest in measuring cortical bone, at sites such as the tibia or radius, has increased during recent years. In osteoporosis the deterioration of bone affects adversely the properties and the effective thickness of the cortical bone wall, and it has been suggested that a multi-site assessment could improve the diagnostic power of ultrasound [48, 36]. However, there are devices from only one manufacturer on the market today for the clinical assessment of long bones. It has become evident that these devices, based on measuring the so-called lateral waves which propagate along the interface of periosteal (outer) bone and soft tissue [16, 11], are relatively insensitive to the changes seen in osteoporosis that occur largely in the endosteal (inner) bone region [31, 89].

The so-called guided waves have been a topic of considerable interest in the field of non-destructive testing, dating back to the 1960’s [110, 109, 106]. Guided waves propagate in bounded media such as plates or layered structures, and carry information of the material properties (e.g. elasticity and density) as well as the geometry (e.g. thickness) of this waveguide [32, 87, 106]. The various applications of guided waves include, e.g., the defect detection or health monitoring of water pipe lines, aircraft wings and different composite laminates [96, 58, 33, 22, 21, 20, 17]. Cortical bone is a plate- or tube-like composite material which might also be expected to support the propagation of guided waves. This could thereby yield an improved ultrasonic assessment of cortical bones, reflecting aspects of the average bone properties throughout the cortical layer. Though only a little attention has been paid to ultrasonic guided wave measurements of human bones [41, 78, 99], recent studies in bone phantoms and animal bones in vitro reflect growing interest in this approach [54, 52].

The purpose of this work was to develop an axial transmission device and methods for measuring guided waves (GW) as well as the first arriving signal (FAS) at approximately 200 kHz central frequency in human bones. This frequency was considerably lower than that used in the currently available commercial axial transmission devices, and thus provided new means for assessing the effects of thickness on the ultrasound velocities. The effect of thickness was verified by comparing phantom measurements with analytical plate theory. The method was tested for the first time on human bones in vitro and in vivo, verifying the relationships between ultrasound velocities and cortical thickness and bone mineral density. Simple plate theory was used here for developing an inversion scheme for estimating the cortical thickness. We also incorporated the tubular shape of bones in the theory, and found thereby a better correspondence between guided wave results and the actual bone properties. In addition, a water-solid bilayer model was used qualitatively to explain the contribution of an overlying soft tissue to in vivo guided wave measurements.

Chapter 2

Bone

2.1 Structure and function

Bone as a material can be classified into organic and inorganic components. The organic material mainly consists of type I collagen and amorphous substance which contains glycoproteins and proteoglycans [8]. The inorganic part of bone is composed of minerals, mostly hydroxyapatite ($Ca_{10}(PO_4)_6(OH)_2$) crystals, and represents about 65% of the wet weight of bone [61, 73]. Together the organic and inorganic components form so-called extracellular bone matrix. Collagen gives bone flexibility, toughness and tensile strength, and also provides loci for nucleation of the mineral crystals which give bone its rigidity and compressive strength [61, 90].

Bone as a tissue consists of cortical and trabecular bone. Cortical (compact) bone forms the majority (approximately 85%) of the bone in the body, and is relatively most abundant is the shafts of the long bones such as the radius, tibia and femur [68]. Cortical bone is relatively dense, with an apparent density of approximately 1.7-2.0 g/cm^3 [85], and this is due to its low porosity (typically 5 - 10%) [14, 61]. The shaft (diaphysis) of the long bones consists of a thick tubular cortex of compact bone surrounding the medullary canal that is filled with bone marrow. The cortical bone wall is composed of osteons (see below) that are aligned parallel to the long axis of bone (Fig. 2.1). This alignment is due to bone's natural ability to organise its structure in order to optimise strength according to different levels of loading applied in different directions. Consequently, cortical bone is anisotropic having the greatest strength and stiffness in the main load-bearing direction, and has a structure designed to resist torsional and bending forces where these occur [14, 61, 101]. Trabecular (cancellous) bone is composed of an interconnected network of bone plates, struts and rods (trabeculae) surrounded by bone marrow. Trabecular bone has essentially the same matrix composition and ultrastructure as compact bone [61], but it has a much higher porosity (50-95%) and consequently a lower apparent density. Trabecular bone absorbs the impact loads and allows bones to broaden near the articular surfaces without the need for excessive increase of bone mass. Trabecular bone can be found at the ends of long bones and in the cores of flat bones. In both cases, the trabecular bone is covered by a thin layer of cortical bone [14].

Bone has a hierarchical architecture with several levels of structure (Figs. 2.1 and 2.2). Mineralised collagen forms long fibrils, which pack together as fibres. In so-called lamellar, or osteonal, bone, collagen fibres organise themselves into planar arrangements called lamellae. The sheets of lamellae wrap as concentric layers around a central canal forming osteons (Haversian systems) with typical diameters ranging from 100 to 300 μm and length 10 mm. The central canal (Haversian canal) of an osteon has a diameter of around 50 μm and contains blood vessels and nerves [61]. The fibres can also form so-called woven bone where fibre orientation is less well distinguished. Woven bone occurs mainly at the early stages of growth and fracture repair. In addition, some of the lamellae do not wrap but remain as planar layers, and together with woven bone form layers of so-called lamellar bone with thickness ranging typically from 150 to 300 μm [86, 14, 61].

The function of bone is to provide mechanical support for the body, as well as to serve as a dynamic mineral reserve and to produce red blood cells. The type of function determines the specific structure of each bone in different parts of the skeleton [14]. Bone at the organ level can be classified into two types: flat bones (skull bones, scapula, mandible, and lileum) and long bones (tibia, femur, humerus, radius, etc.).

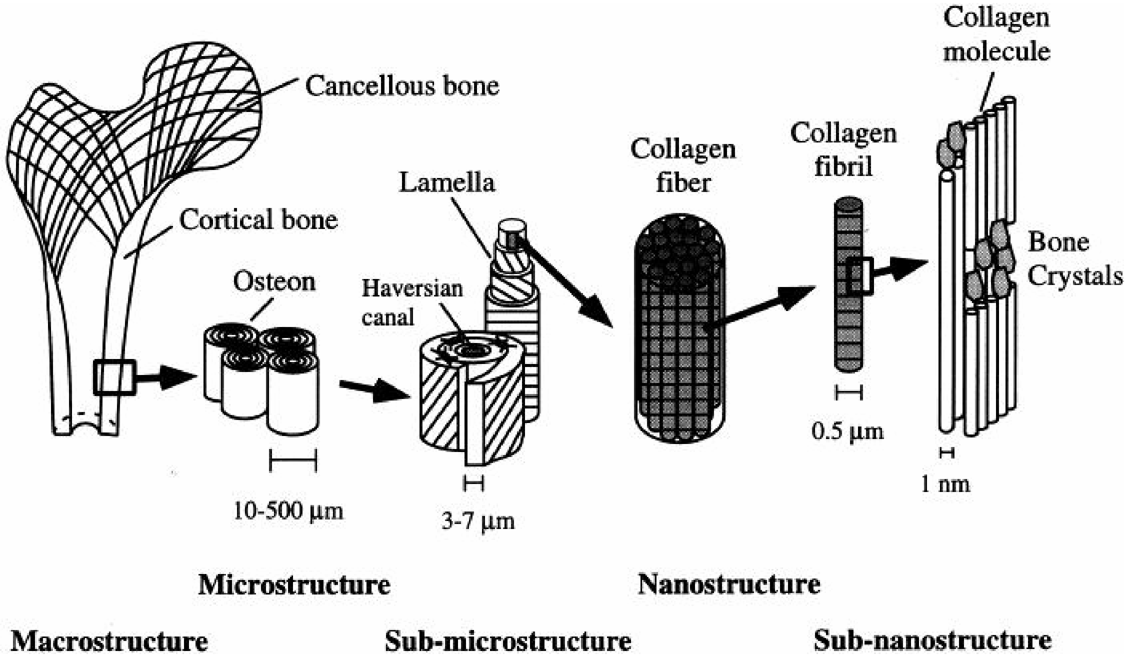

Fig 2.1. Hierarchical structural organisation of bone: (a) cortical and cancellous bone; (b) osteons with Haversian systems; (c) lamellae; (d) collagen fiber assemblies of collagen fibrils; (e) bone mineral crystals, collagen molecules, and non-collagenous proteins (After Rho et al 1998 [86]).

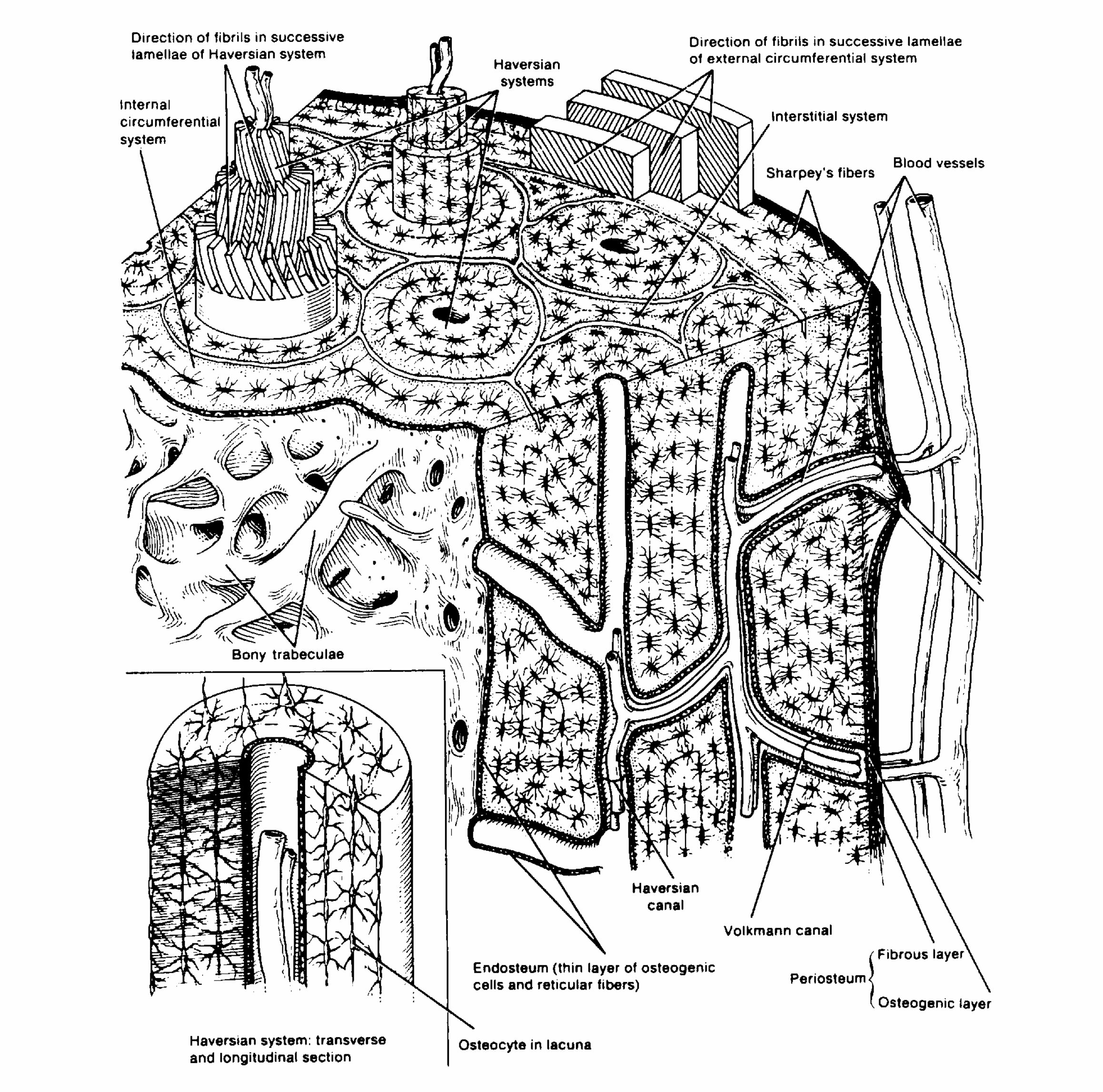

Fig 2.2. Structure of cortical bone (After Buckwalter et al [14]).

2.2 Growth, aging and disease

2.2.1 Bone growth

The growth of bone occurs by two different mechanisms, the so-called endochondral and intramembranous ossification. The former conducts the longitudinal growth, whereas the latter is responsible of the growth in diameter as well as of the remodelling process of the bone tissue [77].

Longitudinal growth takes place in the regions called the growth plate or physis that are located near each end of long bones. In the growth plate new cartilage is constantly formed by chondrocytes. On the side of bone shaft (methaphyseal side) the growth plate mineralises and becomes part of the methaphyseal bone. Consequently, the length of bone shaft is increased while the thickness of the growth plate remains constant. As bones reach their adult length the growth plates are no longer needed and the physes close by ossification [77].

The growth in diameter is another type of mechanism of bone formation, which in addition to growth is also responsible of reshaping the bones. Bone must be removed in some places while it is added to others. This continuous process of bone resorption and formation is known as modelling and it is responsible of the changes both in size and shape. In addition, the architecture of bone must adapt to varying loading conditions and fatigue damage must be repaired throughout the life. These changes are accomplished by a similar removal-replacement process, known as remodelling. The modelling and remodelling refer to actions of osteoblasts and osteoclasts, the former being responsible of formation and the latter of resorption. In modelling these bone cells act independently from each other, whereas remodelling involves coupled actions of these two types of bone cells [68, 61, 15].

2.2.2 Aging

Bone mass is gained through puberty and rises to a peak during the second to third decade [79]. Thereafter, a gradual loss of bone takes place. Women loose about 35-40% of the cortical bone and 55-60% of the trabecular bone whereas in men the bone loss is somewhat smaller by a factor of about a third. As the bone growth stops in the adulthood, this is the point where the peak bone mass is reached. After that, remodelling continues and the rate of loss of bone depends on the balance between bone resorption and formation. The good coupling between these parallel processes is crucially important in order to retain bone mass. Mechanical stimulation of the bone as well as the hormonal effects play important roles in the quality of the coupling. During the normal aging process the coupling weakens and bone balance tends always towards the negative side. This means that the bone mass begins to slowly decrease from that of the peak level reached during the period of growth [79, 73].

2.2.3 Disease

The most common metabolic bone diseases are osteoporosis and osteomalalcia. The currently-accepted definition of osteoporosis, as set out by the National Institute of Health Consensus Conference of 1993, is that osteoporosis is “a disease characterized by low bone mass and microarchitectural deterioration of bone tissue, leading to enhanced bone fragility and a consequent increase in fracture risk” [2]. Osteoporosis typically develops over a long period of time without necessarily causing any symptoms. The first symptoms are fractures caused by minor trauma. The insidious nature of osteoporosis, coupled with the absence of effective therapies capable of replacing bone once it has been lost, makes it a severe and problematic disease.

It has been estimated that 54% of postmenopausal white females in the United States have osteopenia (pre-stage of osteoporosis), and another 30% have osteoporosis [103]. In Finland, the impact of osteoporosis can be seen in the age-adjusted incidence of low-trauma ankle fractures which rose in both women (from 66 in 1970 to 174 in 2000, a 164% increase) and men (from 38 in 1970 to 114 in 2000, a 200% increase) [43]. The most serious complication resulting from osteoporosis is fracture of the hip. The number of hip fractures in Finnish people aged 50 or more has risen from 1857 in 1970 to 7122 in

1997 [42]. The average 1-year total costs of a patient with a hip fracture were Euro 14,410, with about one quarter of these costs being expended on acute care [76]. This gives some idea of the significance of osteoporosis as a public health challenge.

Several subtypes of osteoporosis can be distinguished. Involutional osteoporosis, meaning gradual and progressive bone loss, can be one of two types: postmenopausal osteoporosis and senile osteoporosis [88]. Postmenopausal osteoporosis affects women and occurs mainly between the ages of 50 and 65 years. With this condition, resorption of trabecular bone is accelerated due to oestrogen deficiency associated with the menopause, and this often manifests in wrist and/or spine fracture. Senile osteoporosis occurs both in men and women aged 70 years and older, with a loss of both trabecular and cortical bone, manifesting in fractures of the hip, proximal humerus, tibia and pelvis [88]. So-called secondary osteoporosis is osteoporosis that is caused by factors such as chronic diseases, malabsorption, endocrine disorders, or use of drugs such as corticosteroids. The progress of osteoporosis can be slowed down by proper nutrition and physiological exercise as well as by appropriate medication, such as hormone replacement therapy or bisphosphonate treatment [55].

In osteoporosis, the porosity of bone increases and consequently its apparent density decreases [25]. In trabecular bone, architectural changes occur such as the loss of trabecular struts and perforation of plates. In cortical bone, bone loss occurs mainly in the endosteal region so that the marrow cavity expands and consequently the effective thickness of the compact bone decreases [88].

Osteomalacia is also a metabolic bone disease that occurs as defects in the amount or quality of the mineralization of bone matrix. Thus, osteomalacia can be characterised by relative deficiency of mineral in relation to collagen, which distinguishes it from osteoporosis in which a normal mineral to collagen ratio is observed [103]. Deficiencies of vitamin D, calcium, or phosphorus due to inadequate nutritional intake are the usual causes of osteomalacia [46].

In addition, there are several skeletal disorders which related to genetic, developmental, and dysplastic problems, such as osteogenesis imperfecta, ostosclerosis, and fibrous dysplasia. Osteogenesis imperfecta is a heritable disorder of connective tissue that is caused by abnormalities in type I collagen [84]. Consequently the elastic abilities of the extracellular matrix weaken and bone becomes brittle [105].

2.3 Mechanical properties of bone

The primary function of skeleton is to provide mechanical support for the body in locomotion and static loading. To this end, bone is an adaptive tissue and has optimal mechanical properties, specific to each part of the skeleton. The mechanical properties of bone can be distinguished as the mechanical behaviour of the bone tissue as a material and as the mechanical behaviour of the whole bone as a structure. The material behaviour reflects the intrinsic properties of the bone material itself, being independent of the shape and size of the actual bone. The material properties can be determined by performing mechanical tests on standardised specimens. In addition to material properties, the structure of bone has an important role in terms of the strength. The structural properties include the effect of bone geometry as well as the material properties. The structural properties can be determined by mechanical testing of the whole bone specimens [37, 13, 61].

In vivo the bone is affected by loading of different origins, including external (ground reaction and impact forces) and internal forces (ligament tension, muscle contraction and bone-on-bone contact forces) [13].

The purpose of mechanical testing is to determine the relationship between loading (force applied to bone) and the magnitude of consequent deformation. When the bone is deformed, its response is to the applied stress $\sigma = F / A$, where A is the cross-sectional area of the bone. The definition of compressive and tensile stresses is thereby identical to that of pressure. However, the loading of solid material can also be tension, shear or torsion, yielding the stresses and deformations in the corresponding directions. The magnitude of a local deformation is given by strain ε (compression, tension) or γ (shear) as deformation Δl per unit length l (Fig 2.3). The stress is generally linearly dependent on the strain (Fig 2.3b), and the slope gives the elastic (or Young’s) modulus E. This region is called the elastic region. When the loading is increased, at a certain point the material begins to undergo permanent deformations, and the stress response ceases to be linear. This point is known as the yield point followed by the yield (or plastic) region. The stress corresponding to the yield point is called the yield strength σ_y of the material. The load that causes complete breakage of the material is known as the ultimate (or failure) load, and the corresponding stress as the ultimate strength σ_u [13, 61].

When performing structural testing of the whole bone, it is typical to measure the deformation against the applied force directly. This measurement yields a corresponding figure to Fig 2.3, but the stress is replaced by the force and strain by the actual deformation. The corresponding slope is then called the stiffness [13].

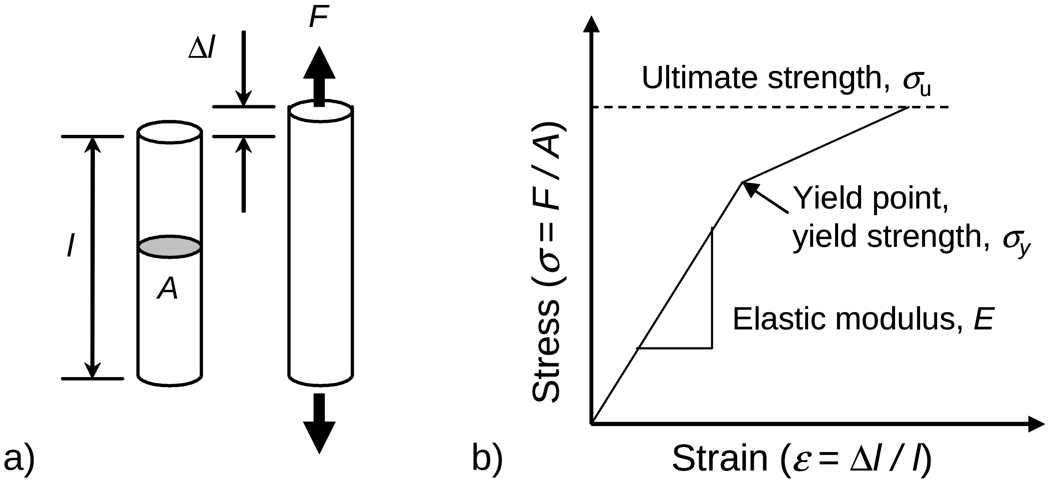

Fig. 2.3. a) A schematic diagram of a tensile loading of a standardised specimen. The test specimen, with length *l* and cross-sectional area *A*, undergoes deformation Δ*l* under loading force *F*. b) A schematic representation of typical stress-strain behaviour under mechanical testing.

Mechanical testing is said to be non-destructive when exploring only the linear elastic region, and the yield point is not reached. The benefit of this approach is that the same specimen remains available for further testing. However, the elastic modulus can be determined more precisely when measuring near the yield point. Also, determination of yield and ultimate strength provides a more complete picture of the mechanical properties of the specimen [13].

If the elastic modulus of the material is independent of the direction of examination, the material is said to be isotropic. In cortical bone, however, the elastic modulus in the direction of the long axis of bone (i.e. the direction of osteons) is approximately two times higher than those in the transverse directions. Thus, cortical bone is anisotropic material. Particularly, it can be modelled using transverse or orthotropic isotropy [5, 39, 81]. The typical longitudinal and transverse elastic moduli of human cortical bone are 17 and 10 GPa, respectively, and the shear modulus is 3.5 GPa [13, 61]. The strength properties of cortical bone depend on the direction also. However, unlike the elastic moduli, the strength is greater in compression than in tension or shear. This alone suggests that the cortical bone has adapted to the conditions where compression loading is greater than tension, and together with the anisotropy, that longitudinally directed loading is greater than transversely directed loading [13].

Unlike those of cortical bone, the mechanical properties of trabecular bone vary a lot depending on the site. For instance, at vertebral bodies the trabecular bone is fairly anisotropic whereas in the femoral head it is nearly isotropic. The elastic modulus of trabecular bone is generally significantly lower than that of cortical bone, ranging roughly within 0.01-10 GPa. These differences in the properties of trabecular bone can indeed be understood due to its adaptation to different loading conditions at different skeletal sites, and the wide range in porosity and microarchitecture adopted to meet these different conditions [13].

Chapter 3

Quantitative ultrasound applied to cortical bone

3.1 The basic physics of ultrasound

Ultrasound is propagation of a mechanical disturbance in a solid or fluid medium at frequencies higher than the upper limit of the audible sound range for humans (~20 kHz). The field of ultrasonics dates back to the end of the 19th and the beginning of the 20th century, when piezoelectricity was discovered and its first applications were developed during the World War I. An in vivo application of bone ultrasound measurement was reported for the first time by Siegel et al in 1958 [94], who used it for monitoring fracture healing in tibia. Today ultrasound has a wide range of medical uses, including diagnostic, therapeutic and surgical applications. Diagnostic ultrasound has several applications, such as non-invasive imaging of different parts of the body and measurement of tissue motion or blood flow. Ultrasound imaging techniques are attractive due to the absence of ionising radiation and the availability of compact devices that provide real time images at lower cost compared to other imaging modalities.

An ultrasound wave emerges as a tiny disturbance of the medium particles around their equilibrium positions, as the matter is excited by a mechanical impulse or vibration. The medium can be considered as a model in which mass points (particles) are connected to each other by strings. Due to the string interactions, the disturbance is transmitted step-by-step to other parts of the medium. The intrinsic elastic properties of the medium, modelled by the strings and particles, define the propagation velocity of the acoustic wave *c*. In the real life, the string constant corresponds to an elastic modulus and particle mass the mass density of the material, which correspondingly define the velocity of the acoustic wave.

The ultrasonic waves can be divided into *longitudinal (compression)* and *shear (transverse) waves*. The longitudinal wave denotes a wave in which the particles oscillate along the longitudinal axis of wave propagation, whereas the shear wave refers to the motion that takes place perpendicularly to the direction of propagation. In perfect fluids (gases or liquids) only longitudinal waves can propagate. Shear waves are not possible because these materials do not support shear forces and the particles are free to slide parallel to each other without any interaction. Elastic solids support both compression and shear motions, thus both of the longitudinal and shear waves can propagate. In a viscous fluid, longitudinal and shear waves can both propagate, but the shear waves are strongly attenuated. Biological soft tissues have similar mechanical properties as viscous fluids, thus in practice only longitudinal waves can propagate in them. Bone is a hard solid tissue in which both longitudinal and shear waves can propagate [51].

In an isotropic solid the speed of the longitudinal wave c_L is given by

$$c_L = \sqrt{\frac{E(1-\nu)}{\rho(1+\nu)(1-2\nu)}}\,, \tag{3.1}$$

where E is Young's modulus, ν Poisson's ratio and ρ the density. Correspondingly, the propagation speed of the shear wave c_T is given by

$$c_T = \sqrt{\frac{\mu}{\rho}}\,, \tag{3.2}$$

where $\mu = E\,/\,2(1+\nu)$ is the shear modulus. c_T is typically less than 0.5 c_L. The velocity of the so-called Rayleigh wave is c_R = 0.9 c_T. The Rayleigh wave propagates along the surface of a semi-infinite medium.

The characteristic acoustic impedance of the medium, Z, is determined as

$$Z = \rho c\,. \tag{3.3}$$

Reflection and refraction will occur at the boundary between two media with different acoustic impedances. The refraction is governed by Snell's law,

$$\frac{\sin\theta_1}{c_1} = \frac{\sin\theta_2}{c_2}\,, \tag{3.4}$$

where c_1 is the velocity of the incident wave, c_2 that of the transmitted wave and θ_1 and θ_2 the angles of incidence and transmission, respectively.

For longitudinal waves on a planar surface of two ideal fluids, the (intensity) reflection and transmission coefficients R and T are given by [104, 51]

$$R = \frac{I_r}{I_i} = \left(\frac{Z_2\cos\theta_1 - Z_1\cos\theta_2}{Z_2\cos\theta_1 + Z_1\cos\theta_2}\right)^2\,, \tag{3.5}$$

$$T = \frac{I_t}{I_i} = \frac{4Z_1Z_2\cos\theta_1\cos\theta_2}{(Z_2\cos\theta_1 + Z_1\cos\theta_2)^2}\,, \tag{3.6}$$

where I_i, I_r, I_t are the incident, reflected and refracted intensities, and Z_1 and Z_2 are the acoustic impedances of the first and second media. Obviously $T + R = 1$. The amount of energy in the reflected wave depends upon the mismatch in acoustic impedance of the two media. The greater the mismatch, the greater the reflected energy.

When either or both of the media are solids, then the energy of the incident wave, longitudinal or shear, will be converted as reflected and refracted longitudinal and shear waves. The number of possible waves depends on the type and order of the two media. If a fluid-solid interface (e.g. soft tissue and bone) is considered, then the incident longitudinal wave can be reflected only as a longitudinal wave and refracted both as longitudinal and shear waves. For the fluid-solid case, Eqs. (3.5-3.6) are only valid at normal incidence. For other angles of incidence the equations become much more complex [51].

If the medium is inhomogeneous, the primary ultrasonic wave interacts with the boundaries of the particles that have different physical properties than the surrounding medium. This process is called scattering, yielding an emission of secondary (scattered) waves. There are three different mechanisms of scattering. a) If the dimensions of the scattering object are significantly larger than the ultrasonic wavelength, specular reflection takes place and Eqs. (3.4-3.6) can be utilised. b) If object dimensions are significantly smaller than the ultrasonic wavelength, then ultrasound is scattered uniformly in all directions, and the incident wave suffers minor perturbations due to diffraction at the edges. c) If the dimensions of the object are of the same magnitude with the wavelength, the scattered radiation exhibits a complex pattern which depends on the acoustic impedance, shape and dimensions of the object. Only two useful cases are relatively easy to calculate: scattering from a sphere and from a cylinder [65, 100].

The attenuation of an ultrasonic wave is a material property and represents the signal loss due to absorption and scattering by objects with scales too small to be captured by the wave. Ultrasound attenuation is characterised by an exponential decrease of the intensity with propagation distance x,

$$I = I_0 e^{-2\cdot\alpha(f)\cdot x} \,, \tag{3.8}$$

where I_0 is the intensity at $x = 0$ and $\alpha(f)$ is the pressure attenuation coefficient expressed as a function of frequency f. The factor 2 in the exponent results from transforming pressure into intensity, since intensity is proportional to the square of pressure for a plane progressive wave [65, 100, 51]. Other factors such as reflection (interface) losses, beam spreading (diffraction) and mode conversion may contribute to a reduction in the intensity of the signal, but in experimental measurements the effects of these extrinsic factors should be removed where possible.

3.2 Axial transmission

The so-called axial transmission technique has been used to assess long bones for over four decades [94, 30, 102, 16]. With this method an ultrasonic signal is mediated to bone at one point, allowed to propagate along the long axis of bone, and recorded from the same side of the bone at a given distance *r* apart from the emitter (Fig. 3.1). Figure (3.2) illustrates a typical recorded signal as a response to excitation of bone in vitro. The transit time *t* of the first arriving signal is determined, e.g., according to a certain threshold value, or the location of the first maximum, and the velocity v_1 (also called as the apparent speed of sound) of the first arriving signal (FAS) is obtained as the ratio between *r* and *t*.

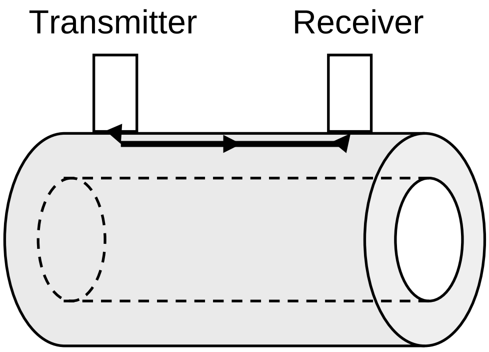

Fig. 3.1. Principle of a typical axial transmission measurement: a transmitter is excited by a pulse or toneburst, a longitudinal wave propagates near the dense periosteal surface of long bone, and this is received as the first arriving signal (FAS) at the receiver.

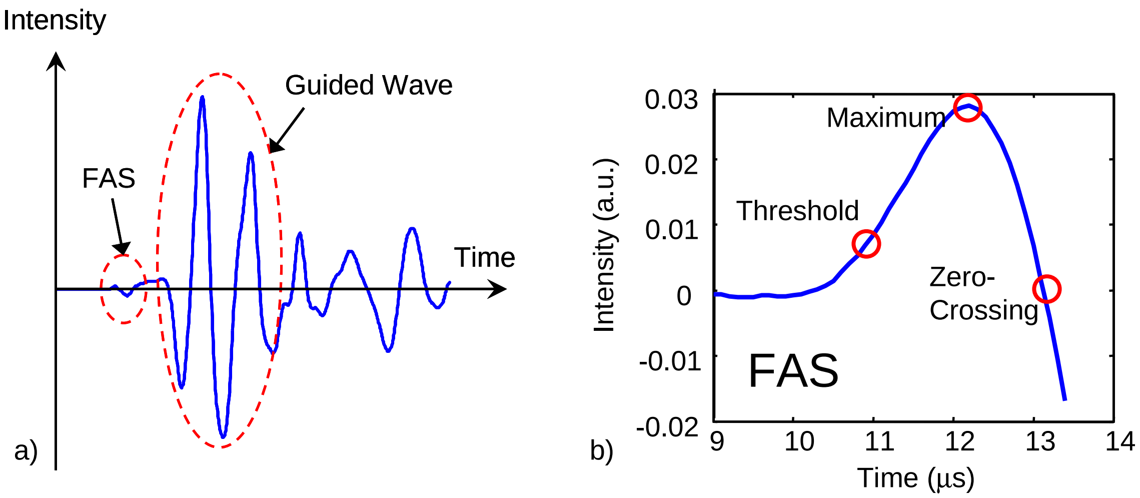

Fig. 3.2. Typical recorded axial ultrasound signal. a) The first arriving signal (FAS) and an additional "guided wave". b) FAS in the close-up. The time-of-flight can be determined according to the first maximum, threshold or zero-crossing point. (Low-frequency axial transmission scanner, human radius in vitro).

Generally, the FAS corresponds to an axial longitudinal wave, provided that the wall thickness h of bone is greater than the acoustic wavelength λ. In bone, the speed of the axial longitudinal wave is approximately 4000 m/s [53, 81].

As the bone is surrounded by soft tissue, the FAS corresponds to the so-called lateral longitudinal (or P-head) wave, which propagates along the interface between these two media [16]. In this case, the excitation is mediated to bone through an overlying soft tissue and the lateral wave is born as a linear wave front which connects the refracted longitudinal wave to the reflected wave. This provided that the incident angle θ_1 is equal to or greater than the critical angle $\theta_c = \sin^{-1}(v_{st}/v_1)$, where v_{st} is ultrasound velocity in the soft tissue (approximately 1500 m/s). The velocity of the lateral wave has been shown to be consistent with that of the longitudinal wave in bone [16], and this essentially enables the clinical measurement of the SOS in bone.

Commercial devices using the axial ultrasound transmission are currently available only from one manufacturer (Sunlight Medical Ltd., Tel Aviv, Israel). These devices operate at a central frequency of 1.25 MHz, which corresponds approximately to a 3 mm acoustic wavelength for the longitudinal waves in bone. It has been demonstrated that the FAS measured under these conditions indeed corresponds to a longitudinal lateral wave that propagates along the dense periosteal (outer) cortical bone [16, 11]. This fact is confirmed by the close agreement between clinically-measured velocities in the human tibia [27, 92, 102, 53, 83, 95] and in vitro measurements of the axial longitudinal wave velocity in human cortical bone specimens [5, 49, 3, 81].

There is, however, evidence indicating that the apparent speed of sound (SOS) is lower than that of the longitudinal wave when the acoustic wavelength λ is greater than the thickness h [74]. Recent numerical simulations and measurements in bone phantoms suggest that the apparent SOS under this condition tends towards that of the fundamental symmetric guided wave (S0 mode) [72, 11, 12]. In vivo studies indeed support this idea that the apparent SOS measured at low ultrasonic frequencies is sensitive to bone thickness. When using a device operating at f = 250 kHz ($\lambda \approx$ 15 mm), a significant correlation between the apparent SOS and bone wall thickness was obtained, whereas in another study using a high-frequency device at f = 1.25 MHz ($\lambda \approx$ 3 mm), no correlation in the tibia and only a modest correlation in the radius was found.

As in the in vivo bone measurements the excitation must be mediated to bone through the overlying soft tissue, and recorded via soft tissue at a given distance r away from the emitter, the consequent delays due to signal passing through the soft tissue must be eliminated (Fig 3.3). This is achieved simply by considering the difference between time delays t_1 and t_2 obtained from consecutive measurements made at two different distances r_1 and r_2, respectively. Now the inverse of v_1 is given by [60]

$$\frac{1}{v_1} = \frac{dt}{dr} , \tag{3.9}$$

where $dt = t_1 - t_2$ and $dr = r_1 - r_2$. The use of multiple transmitter-receiver distances r improves the precision of the velocity v_1 that is determined as an inverse slope through Eq. (3.9) [60].

As discussed above, the soft tissue on top of the bone contributes to the reliability of measuring FAS by affecting the timing of the signal. The delay caused by soft tissue of constant thickness a in the range of consideration can be eliminated using Eq. (3.9) or linear regression. A linearly changing a can easily yield a remarkable bias in the obtained velocities, and this can be reduced using so-called bi-directional approach. The measurement must be performed in both directions yielding v_1^+ and v_1^-, and the actual v_1 is given by

$$\frac{1}{v_1} = \frac{1}{2}\left(\frac{1}{v_1^+} + \frac{1}{v_1^-}\right)\cos\alpha \ , \tag{3.10}$$

where $\alpha = \cos^{-1}((a_1-a_2)/\mathrm{d}r)$ [10]. In addition, soft tissue must be thin enough compared to the emitter-receiver distance r in order to obtain the fastest signal path via bone, i.e. for the given soft tissue thickness a, distance r must be greater than r_{min} defined by [16]

$$r_{\mathrm{min}} = \frac{2a\left(1+\dfrac{v_{st}}{v_1}\right)}{\sqrt{1-\left(\dfrac{v_{st}}{v_1}\right)^2}} \ , \tag{3.11}$$

where v_{st} is ultrasound velocity in the soft tissue.

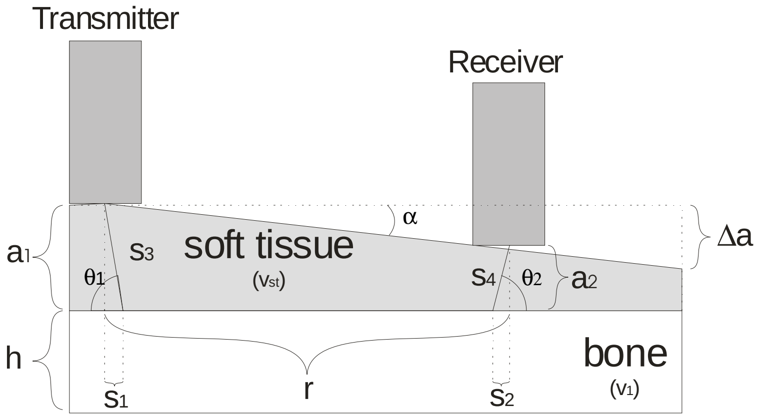

Fig. 3.3. Diagram of an in vivo axial transmission measurement when the thickness *a* of the soft tissue changes linearly.

3.3 Guided waves and bone

In addition to FAS, completely different types of wave modes can also propagate in the long bone (Fig. 3.4). These so-called guided wave modes (GW) propagate, not only in the dense endosteal layer, but throughout the entire cross-section of cortical bone wall in the form of bending waves. As it is known that bone resorption starts in the endosteal bone, and that the consequent decrease of the solid cortical wall thickness yields increased fracture risk (Chapter 2), GW techniques may yield an improved diagnostic bone assessment. However, very little consideration has been given to measuring the GW in bone. A few studies have reported low frequency ultrasonic measurements (f = 100 kHz) of a slow antisymmetric flexural wave in the tibia, mapping the spatial variation in the velocity and quantifying changes during weightlessness [41, 78, 99, 62]. In addition, two recent in vitro studies demonstrated that velocities of guided waves measured in animal bones (f = 100 kHz and f = 50-500 kHz, respectively) correspond with close agreement to guided waves in a plate [54, 52].

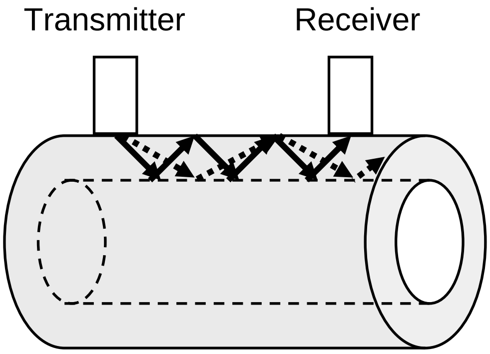

Fig. 3.4. Principle of an axial guided wave measurement. A guided wave arises from multiple reflections at the periosteal and endosteal boundaries, and propagates as a bending vibration of the whole cortical layer.

In general, there is a whole family of different guided wave modes (GW). They arise from reflections, mode conversions and interference of longitudinal and shear waves, and propagate within the boundaries of plate and tube like layered media (Fig 3.4). The velocities of guided waves are functions of wavelength, frequency and layer thickness, and they are in addition determined by the elastic properties and density of the material [106]. These relationships will be treated in more detail in Chapter 4. In terms of the bone application, the endosteal surface of a long bone must be considered as the inner layer and periosteal as the outer layer of a tubular or plate like structure. If either of these assumptions can be made, then ultrasonic waves propagate guided by the bone cortex, and their characteristics are determined by the cortical thickness as well as the elasticity and density of the bone. Potentially, the most interesting guided wave mode regarding the bone applications is the fundamental antisymmetric flexural mode (A0). The velocity of A0 saturates to that of Rayleigh wave in thick layers, but decreases towards zero with decreasing cortical wall thickness.

In addition to the guided wave modes, FAS can also show dispersive behaviour as mentioned in Section 3.2. However, FAS cannot be classified as a pure guided wave mode, but rather as a complicated transition mode between the lateral and fundamental symmetric guided wave (S0), when its wavelength is of the order of or greater than the bone thickness.

The effects of overlying soft tissues are considerably more complicated for guided waves than for FAS, as guided waves cannot usually be considered as bulk waves but preferrably as bending motion of the whole solid layer. The energy propagating in bone can easily leak to surrounding soft tissues causing attenuation and coupling. Coupling between bone and soft tissue means that they form a joint bilayer system in which a guided wave can propagate. Hence, any model of a single bone layer alone cannot very accurately explain the dispersion that takes place in the in vivo measurement of human bone. Thus the bilayer model, which takes the soft tissue coupling into account, will be discussed in Section 4.2.

Chapter 4

Theory of Guided Waves

Though the concept of guided ultrasonic waves is novel in the field of bone quality assessment, guided waves have been widely used for many years in different applications of non-destructive testing for the assessment of plates, tubes and more complex structures [21, 20, 19, 17, 44]. This chapter reviews approaches to the theoretical description of guided waves with particular emphasis on those aspects of the theory relevant to the applications of guided waves for bone assessment.

The propagation of guided waves in solids is governed by partial differential wave equations that arise from theory of elasticity. These governing equations are identical for guided as well as for bulk longitudinal and shear waves. The fundamental difference that distinguishes the guided waves from the bulk waves is that the latter propagate in the bulk of a material, independent of the boundaries, whereas the guided waves are born due to boundary interactions. Guided waves arise due to reflection, refraction, and mode conversion of longitudinal and shear waves at the boundaries of the media resulting in resonant modes whose frequency and propagation speed correspond to standing waves in the thickness direction of the structure. Mathematically, the solution of a guided wave must satisfy a number of boundary conditions, and the introduction of the boundary conditions makes the problem of guided waves difficult to solve. In most cases no analytical solution can be found, and often the use of numerical methods is needed [87].

Classically, the problem of guided waves is associated with waves in a traction-free isotropic plate (Lamb waves) [50, 106]. Due to the complexity of guided wave problems, a solution for the free plate case may be a convenient starting point for understanding the actual application. Sometimes it may be possible to consider the actual structure, e.g. a tubular bone, as a plate within a sufficient precision [54]. It is possible also to generalise the problem to deal e.g. with tubular shape, anisotropy and multilayer structures [32, 87].

4.1 Waves in plates

Lamb waves are two-dimensional elastic waves that propagate in a traction-free solid elastic plate of finite thickness h. They can be modelled using four partial waves, downward and upward propagating longitudinal and shear waves (Fig 4.1).

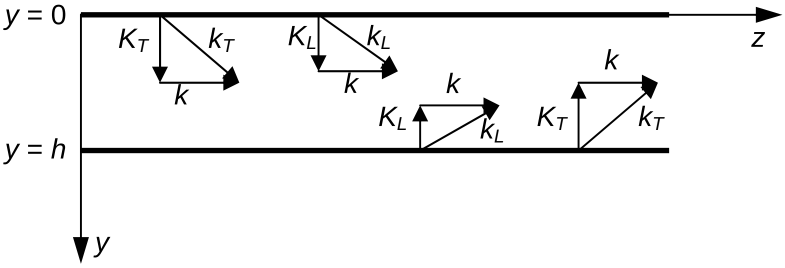

Fig 4.1. Geometry of the free plate problem. Plate thickness is *h*. Lower-case $k_{L,T}$ are respectively the wave numbers of the longitudinal and shear partial waves, capital $K_{L,T}$ are the corresponding vertical wave numbers, and *k* is the wave number of the propagating guided wave.

The motion of a homogeneous, linear elastic solid can be modelled by Navier's displacement equations of motion,

$$(\lambda+\mu)u_{j,ij}+\mu u_{i,jj}=\rho\ddot{u}_i\,, \tag{4.1}$$

where u_i is the displacement vector,

$$u_{k,ij}=\frac{\partial^2}{\partial x_i \partial x_j}u_k\,,$$

ρ is the mass density and λ and μ are the Lamé constants. Summation over a repeated index is assumed. The displacement vector can be expressed via Helmholtz decomposition,

$$u_i=\frac{\partial\phi}{\partial x_i}+e_{ijk}\frac{\partial\psi_k}{\partial x_j}\,, \tag{4.2}$$

where ϕ and ψ_j are scalar and vector potentials, respectively, and e_{ijk} is the permutation symbol. Substitution of Eq. (4.2) into Eq. (4.1) yields two uncoupled wave equations

$$\left(\nabla^2-\frac{1}{(c_L)^2}\frac{\partial^2}{\partial t^2}\right)\phi=0 \quad , \left(\nabla^2-\frac{1}{(c_T)^2}\frac{\partial^2}{\partial t^2}\right)\psi=0\,, \tag{4.3}$$

where $\nabla^2 = \partial^2/\partial y^2 + \partial^2/\partial z^2$, c_L is the bulk longitudinal velocity and c_T the bulk shear velocity. According to the partial wave formalism [87], the solutions of Eqs. (4.3) can be written as

$$\phi=C_1e^{ik_L\left[z\sin(\theta_L)+y\cos(\theta_L)\right]}+C_2e^{ik_L\left[z\sin(\theta_L)-y\cos(\theta_L)\right]} \tag{4.4a}$$

$$\psi=C_3e^{ik_T\left[z\sin(\theta_T)+y\cos(\theta_T)\right]}+C_4e^{ik_T\left[z\sin(\theta_T)-y\cos(\theta_T)\right]}\,, \tag{4.4b}$$

where

$$\theta_L = \arcsin\left(\frac{k}{k_L}\right), \qquad \theta_T = \arcsin\left(\frac{k}{k_T}\right),$$

k_L is the wavenumber of a longitudinal wave component, k_T the wavenumber of a shear wave component and k the wavenumber of a guided wave (in the direction of propagation) (Fig 4.1). The constants C_1, C_2, C_3 and C_4 are arbitrary unknowns and will be determined by the boundary conditions.

Both of the potentials in Eqs. (4.4) now consist of two terms, one representing a downward propagating plane wave (positive y in the exponential term) and one representing an upward propagating plane wave (negative y in the exponential term). Technically we have thus assumed that there are four plane bulk waves in the solid, two longitudinal and two shear (Fig 4.1).

Displacements u_i can now be obtained from Eq. (4.2), and stresses σ_{ij} are given by

$$\sigma_{ij} = \lambda\delta_{ij}\varepsilon_0 + 2\mu\varepsilon_{ij}, \tag{4.5}$$

where δ_{ij} is the Kronecker delta, the dilation is $\varepsilon_0 = \varepsilon_{11} + \varepsilon_{22} + \varepsilon_{33}$, and the strains are

$$\varepsilon_{ij} = \frac{1}{2}\left(\frac{\partial u_i}{\partial x_j} + \frac{\partial u_j}{\partial x_i}\right). \tag{4.6}$$

By requiring traction-free boundary conditions, $\sigma_{yy} = \sigma_{yz} \equiv 0$ at the free plate surfaces $y = 0$ and $y = h$, where h is the plate thickness, and ignoring the shear horizontal displacements ($u_x \equiv 0$), four equations will be obtained,

$$\left(\lambda k_L^2 + 2\mu K_L^2\right)\left\{C_1 + C_2\right\} + 2\mu k K_T\left\{C_3 - C_4\right\} = 0, \tag{4.7a}$$

$$-2\mu k K_L\left\{C_1 - C_2\right\} + \mu\left(K_T^2 - 2k_T^2\right)\left\{C_3 + C_4\right\} = 0, \tag{4.7b}$$

$$\left(\lambda k_L^2 + 2\mu K_L^2\right)\left\{C_1 e^{iK_L h} + C_2 e^{-iK_L h}\right\} + 2\mu k K_T\left\{C_3 e^{iK_T h} - C_4 e^{-iK_T h}\right\} = 0, \tag{4.7c}$$

$$-2\mu k K_L\left\{C_1 e^{iK_L h} - C_2 e^{-iK_L h}\right\} + \mu\left(K_T^2 - 2k_T^2\right)\left\{C_3 e^{iK_T h} + C_4 e^{-iK_T h}\right\} = 0, \tag{4.7d}$$

where

$$K_{L,T} \equiv k_{L,T}\cos(\theta_{L,T}) = \sqrt{k_{L,T}^2 - k^2} = \sqrt{\left(\frac{\omega}{c_{L,T}}\right)^2 - k^2},$$

and ω is the angular frequency.

This system of equations, Eqs. (7a-7d), can be expressed in a matrix form

$$[G]\{C\} = 0, \tag{4.8}$$

where $[G]$ is the global matrix,

$$[G] = \begin{bmatrix} \lambda k_L^2 + 2\mu K_L^2 & \lambda k_L^2 + 2\mu K_L^2 & 2\mu k K_T & -2\mu K_T \\ -2\mu k K_L & 2\mu k K_L & \mu\left(K_T^2 - 2k_T^2\right) & \mu\left(K_T^2 - 2k_T^2\right) \\ \left(\lambda k_L^2 + 2\mu K_L^2\right)e^{iK_L h} & \left(\lambda k_L^2 + 2\mu K_L^2\right)e^{-iK_L h} & 2\mu k K_T e^{iK_T h} & -2\mu k K_T e^{-iK_T h} \\ -2\mu k K_L e^{iK_L h} & 2\mu k K_L e^{-iK_L h} & \mu\left(K_T^2 - 2k_T^2\right)e^{iK_T h} & \mu\left(K_T^2 - 2k_T^2\right)e^{-iK_T h} \end{bmatrix},$$

and vector $\{C\}$ contains the four unknown constants C_i, i = 1,…,4. The matrix equation Eq. (4.8) is satisfied when the determinant of matrix $[G]$ vanishes. The characteristic equation for a plate in vacuum (with given wavenumber k, angular frequency ω, bulk velocities c_L and c_T, and plate thickness h) can thus be written as

$$\det\left(G\left(\omega, k, c_L, c_T, h\right)\right) = 0\,. \tag{4.9}$$

The roots of this characteristic (or dispersion) equation provide the dispersion relations for the given structure, and can be solved numerically [87, 59, 80].

The technique described above is known as the global matrix method. Though not as elegant as the classical solution for Lamb waves [50, 106, 32], it is powerful as the global matrix $[G]$ can easily be extended to different multilayer plate and tube structures. This is a useful property, for instance, if attempting to model the coupling effects of a soft (e.g. liquid) overlayer on top of bone or bone phantoms (see section 4.2).

Classically, the solutions of Eq. (4.3) are sought in forms [32]

$$\begin{aligned} \phi &= f(y)e^{i(kx-\omega t)}\,, \\ \psi &= ih(y)e^{i(kx-\omega t)}, \end{aligned} \tag{4.10}$$

where $f(y) = C_1 \sin(K_L y) + C_2 \cos(K_L y)$ and $h(y) = C_3 \sin(K_T y) + C_4 \cos(K_T y)$. Here the exponential term represents the propagating wave in the axial (horizontal) direction, and $f(y)$ and $h(y)$ standing waves in the vertical direction. The displacements, strains and stresses are obtained from Eqs. (4.2), (4.6) and (4.5), and requiring the traction-free boundary conditions $\sigma_{yy} = \sigma_{yz} \equiv 0$ at the free plate surfaces ($y = \pm h/2$, for convenience) consequently yields the classical Rayleigh-Lamb frequency equation

$$\frac{\tan(2K_T h)}{\tan(2K_L h)} + \left\{\frac{4K_L K_T k^2}{\left(k^2 - K_T^2\right)^2}\right\}^{\pm 1} = 0\,. \tag{4.11}$$

This equation divides in two parts that correspond to axially symmetric modes (+1) and antisymmetric modes (-1). The dispersion relations of Eq. (4.11) are identical with those of Eq. (4.8), and must also be solved numerically.

4.2 Fluid-solid bilayer

The purpose of developing a model for Lamb waves in a fluid-solid bilayer was to explain the effect of soft tissue on top of the bone. In this model the liquid on top of a solid plate played the role of soft tissue.

The problem of a fluid-solid bilayer has been discussed comprehensively e.g. by Yapura and Kinra [111]. At an interface between solid and fluid the energy of guided waves leaks from solid to fluid in the form of leaky waves. The leaky waves, however, are reflected back at the top boundary of the thin fluid overlayer and propagate back to the solid substrate. As a consequence the guided waves propagate, not in the fluid or solid layer alone, but in the whole bilayer structure. This coupling affects strongly the dispersion characteristics of the guided wave modes. As this kind of coupling is expected when there is a layer of soft tissue on top of bone (in vivo measurements), a bilayer model is needed in the analysis of measurement results.

Yapura and Kinra [111] developed a bilayer counterpart to Eq. (4.11) using the classical approach. In the following, however, the partial wave formalism will be used to extend the global matrix of the solid plate (Eq. 4.8) into the fluid-solid bilayer case [87].

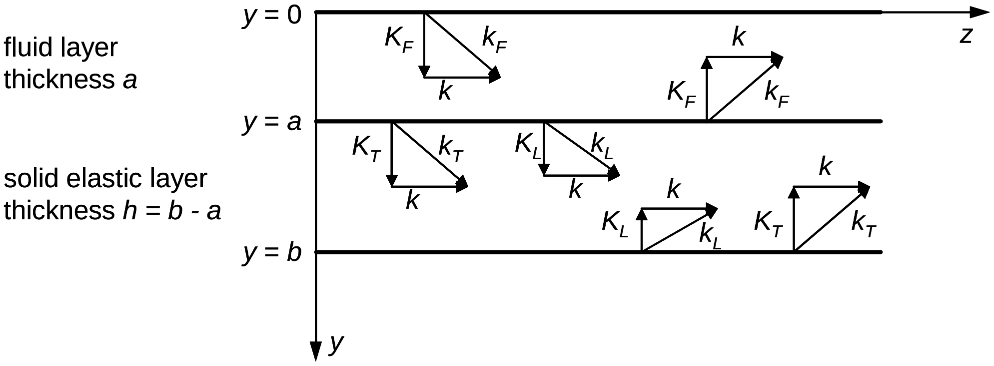

Fig. 4.2. Geometry of the fluid-solid bilayer plate problem. Lower-case $k_{L,T,F}$ are respectively the wave numbers of the longitudinal, shear and fluid partial waves, capital $K_{L,T,F}$ are the corresponding vertical wave numbers, and k is the wave number of the guided wave.

The ideal fluid can be treated similarly than the elastic solid, except that fluid only sustains longitudinal waves. As in the solid we had four partial waves, the fluid overlayer increases the number of partial waves by two (Fig 4.2).

The wave equation for the fluid is given by

$$\left(\nabla^2 - \frac{1}{(c_F)^2}\frac{\partial^2}{\partial t^2}\right)\phi_F = 0, \tag{4.12}$$

where ϕ_F is the scalar potential, $c_F = \lambda_F/\rho_F$ is the bulk velocity, and λ_F and ρ_F are respectively the bulk modulus and density of the fluid. The scalar potential ϕ_F can be expressed analogously to Eq. (4.4a), when replacing the sub-index L with F. The vector potential $\psi_F = 0$. The corresponding displacements u_{iF}, strains ε_{ijF} and stresses σ_{ijF} can be obtained from Eqs. (4.2), (4.6) and (4.5).

The six boundary conditions that must be satisfied are

$$\begin{aligned}
&\sigma_{yyF}\big|_{y=0} = 0 \\
&u_{yF}\big|_{y=a} = u_y\big|_{y=a} \\
&\sigma_{yyF}\big|_{y=a} = \sigma_{yy}\big|_{y=a} \\
&\sigma_{yz}\big|_{y=a} = 0 \\
&\sigma_{yy}\big|_{y=a+h} = 0 \\
&\sigma_{yz}\big|_{y=a+h} = 0.
\end{aligned} \tag{4.13}$$

These boundary conditions yield six boundary condition equations that can by expressed in the matrix form

$$[G]\{C\} = 0, \tag{4.14}$$

where $[G]$ is the global matrix and $\{C\}$ the vector of six unknowns C_{i}, i = 1,…,6. The elements of the matrix $[G]$ are given by

$$\begin{aligned}
&G_{11} = -\lambda_F k_F^2 && G_{41} = 0 \\
&G_{12} = -\lambda_F k_F^2 && G_{42} = 0 \\
&G_{13} = 0 && G_{43} = -2\mu k K_L e^{iK_L a} \\
&G_{14} = 0 && G_{44} = 2\mu k K_L e^{-iK_L a} \\
&G_{15} = 0 && G_{45} = \mu\left(K_T^2 - k^2\right)e^{iK_T a} \\
&G_{16} = 0 && G_{46} = \mu\left(K_T^2 - k^2\right)e^{-iK_T a} \\
&G_{21} = K_F e^{iK_F a} && G_{51} = 0 \\
&G_{22} = -K_F e^{-iK_F a} && G_{52} = 0 \\
&G_{23} = -K_L e^{iK_L a} && G_{53} = \left(\lambda k_L^2 + 2\mu K_L^2\right)e^{iK_L(a+h)} \\
&G_{24} = K_L e^{-iK_L a} && G_{54} = \left(\lambda k_L^2 + 2\mu K_L^2\right)e^{-iK_L(a+h)} \\
&G_{25} = -k e^{iK_T a} && G_{55} = 2\mu k K_T e^{iK_T(a+h)} \\
&G_{26} = -k e^{-iK_T a} && G_{56} = -2\mu k K_T e^{-iK_T(a+h)} \\
&G_{31} = \lambda_F k_F^2 e^{iK_F a} && G_{61} = 0 \\
&G_{32} = \lambda_F k_F^2 e^{-iK_F a} && G_{62} = 0 \\
&G_{33} = -\left(\lambda k_L^2 + 2\mu K_L^2\right)e^{iK_L a} && G_{63} = 2\mu k K_L e^{iK_L(a+h)} \\
&G_{34} = -\left(\lambda k_L^2 + 2\mu K_L^2\right)e^{-iK_L a} && G_{64} = -2\mu k K_L e^{-iK_L(a+h)} \\
&G_{35} = -2\mu k K_T e^{iK_T a} && G_{65} = -\mu\left(K_T^2 - k^2\right)e^{iK_T(a+h)} \\
&G_{36} = 2\mu k K_T e^{-iK_T a} && G_{66} = -\mu\left(K_T^2 - k^2\right)e^{-iK_T(a+h)}.
\end{aligned} \tag{4.15}$$

Equation (4.14) is satisfied when the determinant of the global matrix $[G]$ vanishes. The dispersion equation for the fluid-solid bilayer can thus be written as

$$\det\left(G\left(\omega, k, c_F, c_L, c_T, a, h, \rho_F, \rho\right)\right) = 0\,. \tag{4.16}$$

where c_L and c_T are respectively the bulk longitudinal and shear velocities, ρ the density, h the thickness of the solid substrate, c_F the bulk velocity, ρ_F the density and a the thickness of the fluid overlayer. The roots of Eq. (4.16) must be solved numerically.

4.3 Effect of anisotropy

The anisotropy of cortical bone has been studied by several researchers and experimental results for the anisotropy of the elastic constants have been reported [5, 39, 81]. Long bones can be considered transversely isotropic or orthotropic. In addition, the effect of anisotropy on the propagation of guided waves is well known e.g. in non-destructive testing of composite laminates [87, 80, 69, 70, 34]. However, the incorporation of anisotropy in the guided wave model of bone is as yet unexplored.

This study did not include an extensive consideration of bone anisotropy. We, however, briefly comment here, how to incorporate anisotropy in the Lamb wave theory.

The fundamental difference between the treatment of wave propagation in an isotropic and an anisotropic medium is that in the anisotropic case the governing equations of motion cannot be expressed as two simple equations, as Eqs. (4.3), by substituting the displacements u_i to the equations of motion using the Helmholtz decomposition, Eq. (4.2). As it is not convenient to use this so-called method of potentials (Helmholtz decomposition is a function of the scalar and vector potential) for the anisotropic materials, a more general solution is often considered [87].

For zero body forces, the propagation of elastic waves in anisotropic media is governed by the equation [87]

$$C_{ijkl} = \frac{\partial^2 u_k}{\partial x_j x_l} = \rho \frac{\partial^2 u_i}{\partial t^2}\,, \tag{4.17}$$

where C_{ijkl} is the elastic tensor, which defines the elastic constants and the anisotropy for the medium. A single guided wave mode in an anisotropic plate is composed of six partial waves (instead of four for an isotropic plate), whose displacements u_i can be expressed as

$$u_i = \alpha_i \ \exp[ik(z + l_y y)]\exp[-i\omega t]\,, \tag{4.18}$$

where the α_i are the amplitudes and $l_y = k_y/k_z$ is the ratio of vertical to axial wave number. Each of these partial waves satisfies the homogeneous Eq. (4.17), and the substitution of Eq. (4.18) into Eq. (4.17) allows to determine the $l_y^{(n)}$ for each partial wave modes $n = 1, 2, \ldots, 6$. Requiring traction-free boundary conditions $\sigma_{yy} = \sigma_{yz} = \sigma_{yx} \equiv 0$ at the upper and lower boundaries of the plate, then finally yields the characteristic dispersion equation for an anisotropic plate [87].

4.4 Effect of tubular shape

The problem of guided waves in tubes has been a topic of considerable interest in non-destructive testing [112, 64, 96, 107, 108, 80, 18, 47, 4, 67, 34], but no extensive studies have been made considering the bone application.

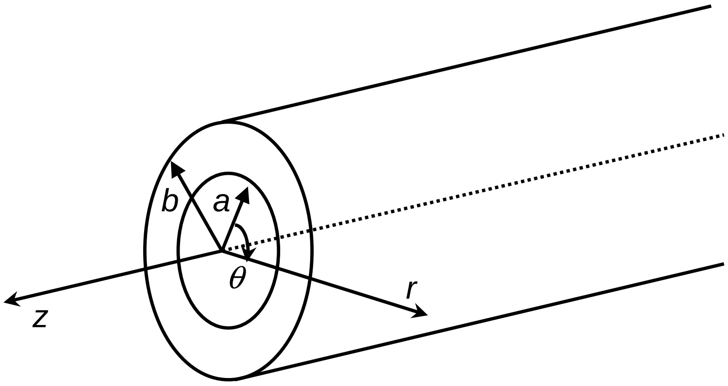

Fig. 4.3. Geometry of the free tube problem, *a* is the inner and *b* the outer radius.

The exact solutions to the axially propagating guided waves in hollow traction-free tubes were first published by Gazis [29], and followed e.g. by Graff [32], Pavlakovic [80] and Rose [87]. In tubes the guided waves must be modelled in three dimensions, whereas two-dimensional modelling was sufficient for an isotropic plate. It is convenient to consider the tube problem in cylindrical coordinates r, θ and z (Fig 4.3).

The traction-free boundary conditions are

$$\sigma_{rr} = \sigma_{r\theta} = \sigma_{rz} = 0 \quad \text{at} \quad r = a, \text{ and } \ r = b. \tag{4.19}$$

The assumed radial, circumferential and axial displacement components can respectively be given by

$$\begin{aligned} u_r &= U_r(r)\cos n\theta \cos(\omega t + kz), \\ u_\theta &= U_\theta(r)\sin n\theta \cos(\omega t + kz), \\ u_z &= U_z(r)\cos n\theta \sin(\omega t + kz), \end{aligned} \tag{4.20}$$

where n = 0, 1, 2, 3, … is the circumferential order, and U_r, U_θ and U_z are the corresponding displacement amplitudes composed of Bessel and modified Bessel functions.

When considering the axial transmission, i.e. wave propagation along the long axis of the tube, the guided waves modes can be divided into three classes [112, 96]:

longitudinal modes	$L(0, m)$	(axisymmetric modes),
torsional modes	$T(0, m)$	(axisymmetric modes),
flexural modes	$F(n, m)$	(non-axisymmetric modes).

Here n = 1, 2, 3, … is the circumferential order and m = 1, 2, 3, … is the number of mode [87]. The counterpart of the fundamental antisymmetric plate mode (A0), which we have mostly been interested in regarding the bone application, is the fundamental flexural tube mode $F(1,1)$ (hereafter referred to as F11).

The dispersion equation for the hollow traction-free tube can be expressed as

$$\det([G]) = 0\,, \tag{4.21}$$

where $[G]$ is a six-by-six global matrix. The first three rows of the matrix elements are [87]:

$$\begin{aligned}
G_{11} &= [2n(n-1) - (\beta^2 - k^2)a^2]Z_n(\alpha a) + 2\gamma_1 \alpha a Z_{n+1}(\alpha a),\\
G_{12} &= 2k\beta a^2 Z_n(\beta a) - 2ka(n+1)Z_{n+1}(\beta a),\\
G_{13} &= -2n(n-1)Z_n(\beta a) + 2\gamma_2 n\beta a Z_{n+1}(\beta a),\\
G_{14} &= [2n(n-1) - (\beta^2 - k^2)a^2]W_n(\alpha a) + 2\alpha a W_{n+1}(\alpha a),\\
G_{15} &= 2\gamma_2 k\beta a^2 W_n(\beta a) - 2ka(n+1)W_{n+1}(\beta a),\\
G_{16} &= -2n(n-1)W_n(\beta a) + 2n\beta a W_{n+1}(\beta a),\\[4pt]
G_{21} &= 2n(n-1)Z_n(\alpha a) - 2\gamma_1 n\alpha a Z_{n+1}(\alpha a),\\
G_{22} &= -k\beta a^2 Z_n(\beta a) + 2ka(n+1)Z_{n+1}(\beta a),\\
G_{23} &= -[2n(n-1) - \beta^2 a^2]Z_n(\beta a) - 2\gamma_2 \beta a Z_{n+1}(\beta a),\\
G_{24} &= 2n(n-1)W_n(\alpha a) - 2n\alpha a W_{n+1}(\alpha a),\\
G_{25} &= -\gamma_2 k\beta a^2 W_n(\beta a) + 2ka(n+1)W_{n+1}(\beta a),\\
G_{26} &= -[2n(n-1) - \beta^2 a^2]W_n(\beta a) - 2\beta a W_{n+1}(\beta a),\\[4pt]
G_{31} &= -2nkaZ_n(\alpha a) + 2\gamma_1 k\alpha a^2 Z_{n+1}(\alpha a),\\
G_{32} &= -n\beta a Z_n(\beta a) + (\beta^2 - k^2)a^2 Z_{n+1}(\beta a),\\
G_{33} &= nkaZ_n(\beta a),\\
G_{34} &= -2nkaW_n(\alpha a) + 2k\alpha a^2 W_{n+1}(\alpha a),\\
G_{35} &= -\gamma_2 n\beta a W_n(\beta a) + (\beta^2 - k^2)a^2 W_{n+1}(\beta a),\\
G_{36} &= nkaW_n(\beta a),
\end{aligned} \tag{4.22}$$

where Z_n and W_n represent incoming and outgoing Bessel functions, k is the axial wavenumber, μ one of the Lamé constants, $\alpha^2 = \omega^2/c_L^2 - k^2$, $\beta^2 = \omega^2/c_T^2 - k^2$, $\alpha = (|\alpha^2|)^{½}$, and $\beta = (|\beta^2|)^{½}$. The remaining matrix elements, G_{41} to G_{66}, are obtained from elements G_{11} to G_{36} by replacing a with b in Eq. (4.22). The proper criteria for choosing the Bessel functions can be found in Table 4.1. The incoming wave Z_n can be substituted by the Bessel function J_n or modified Bessel function I_n, and the outgoing wave W_n by the Bessel function Y_n or modified Bessel function K_n. Parameters γ_1 and γ_2 account for differences in the recurrence relationships of different Bessel functions (Table 4.1).

The roots of Eq. (4.21) yield the dispersion relations of a free tube and they must be solved numerically. The principle of a numerical solution routine is described in Section 4.5.

Table 4.1. Criteria for choosing the appropriate Bessel functions.

$\alpha^2 > 0$ and $\beta^2 > 0$	$\alpha^2 < 0$ and $\beta^2 > 0$	$\alpha^2 < 0$ and $\beta^2 < 0$
$\gamma_1 = 1$ $\gamma_2 = 1$ $Z_n(\alpha r) = J_n(\alpha r)$ $W_n(\alpha r) = Y_n(\alpha r)$ $Z_n(\beta r) = J_n(\beta r)$ $W_n(\beta r) = Y_n(\beta r)$	$\gamma_1 = -1$ $\gamma_2 = 1$ $Z_n(\alpha r) = I_n(\alpha r)$ $W_n(\alpha r) = K_n(\alpha r)$ $Z_n(\beta r) = J_n(\beta r)$ $W_n(\beta r) = Y_n(\beta r)$	$\gamma_1 = -1$ $\gamma_2 = -1$ $Z_n(\alpha r) = I_n(\alpha r)$ $W_n(\alpha r) = K_n(\alpha r)$ $Z_n(\beta r) = I_n(\beta r)$ $W_n(\beta r) = K_n(\beta r)$

4.5 Implementation of numerical solution

The dispersion equations of guided waves, such as (Eq. 4.9), cannot be solved analytically but a numerical solution must be used. In order to find a point on a dispersion curve, a root of the characteristic equation (Eq. 4.9) must be found. A root corresponds to a point where the determinant of the complex-valued global matrix [G] is zero. The coefficients of matrix [G] depend on the geometry of the system (e.g. plate thickness h), material properties (e.g. c_L and c_T), frequency f, real wave number k and attenuation coefficient α.. The latter three, f, k and α, must be varied in order to find valid roots.

If the materials are elastic and the waveguide is considered as free in the vacuum, as it was the case in this study, then there is no way for energy to leave the system and the attenuation will be zero. This simplifies the root search as the roots will be real. In the case when attenuation is involved, the roots will be complex and a more complicated two-dimensional root search routine is required. The imaginary part of the complex wave number corresponds to the attenuation coefficient α.

Figure 4.4 illustrates one example of a surface corresponding to the magnitude of det([G]) drawn in logarithmic absolute scale. The minima observed in this surface correspond to the roots (c_p^i,f_i) of the dispersion equation, and they determine the trajectories of the dispersion curves. The phase velocities c_p^i can be obtained from the wave numbers by $c_p^i = 2\pi \cdot f_i \,/\, k_i$, and it is a matter of choice whether to consider the problem in terms of c_p^i or k_i.

An efficient method used for tracing the trajectories of the dispersion curves was adopted from Lowe [59] and Pavlakovic [80]. The procedure was started with a frequency sweep, followed by curve tracing routines. The frequency sweep sought for the minima f of abs(det([G])) (Fig. 4.1) for given c_p or k, and then the exact f were determined using the Newton-Raphson algorithm. The points obtained from the frequency sweep were used as the starting points in tracing the individual curves. In the curve tracing routine, the starting point was used as the first initial guess, and as the number of obtained roots increased, linear or quadratic extrapolation was used for predicting the next points that fall on the trajectory of the sought dispersion curve. The use of extrapolation made this process efficient and robust, increasing the precision of the initial guess.

The curve trace yielded the dispersion curves in terms of *f*, *k*, and c_p. The corresponding group velocities were obtained by $c_g = 2\pi \cdot df / dk$.

Some examples of the dispersion curves for plate, fluid-solid bilayer and tube structures are shown in Figure 4.5. The curves were computed using parameters similar to those of cortical bone.

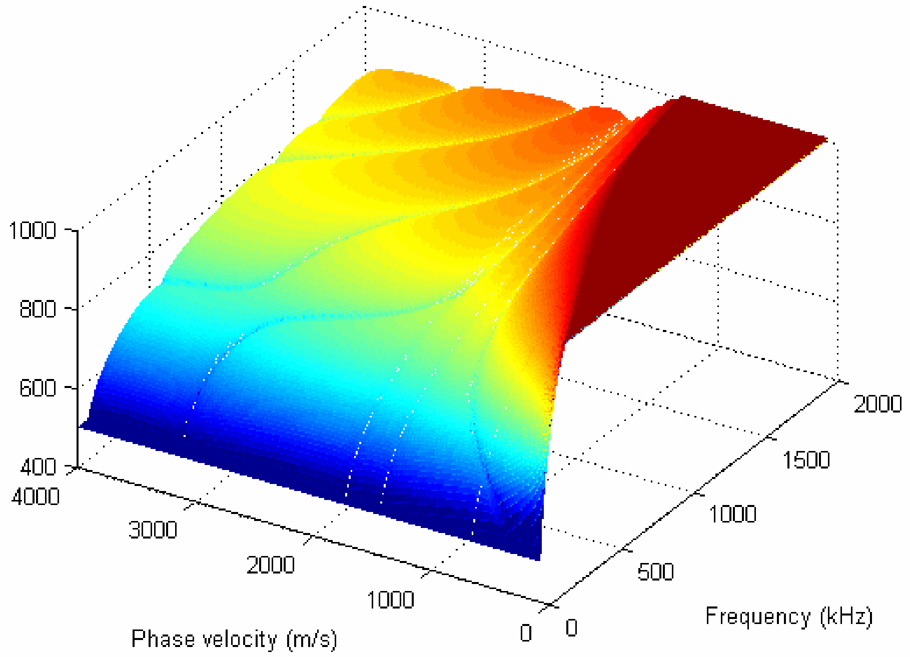

Fig. 4.4. The magnitude of the determinant of the global matrix [*G*] illustrated in logarithmic absolute scale. The minima of the surface correspond to the roots of the dispersion equation and determine the dispersion curves.

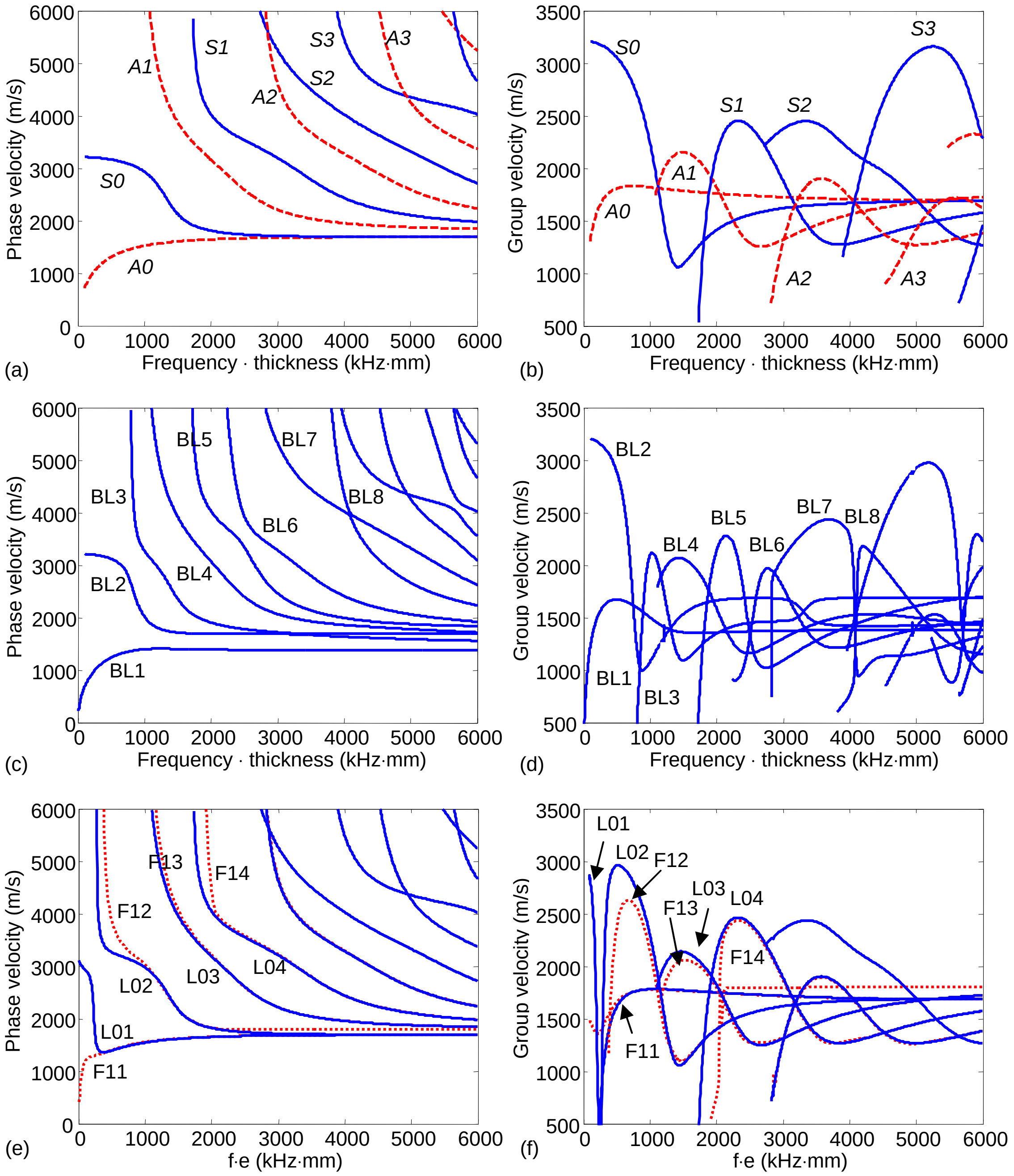

Fig. 4.5. Phase and group velocity dispersion curves respectively for a), b) a free isotropic plate, c), d) a fluid-solid bilayer and e), f) a free hollow tube. Material properies were c_L = 4000 m/s, c_T = 1800 m/s, c_F = 1500 m/s, ρ = 2.0 g/cm^3, ρ_F = 1.0 g/cm^3. The fluid to solid thickness ratio was 0.5 (c,d) and the wall thickness to outer radius ratio was 0.4 (e,f).

Chapter 5

Experimental and numerical methods

5.1 Device

Experimental measurements were performed using an axial pulse transmission scanner with a pair of unfocussed low-frequency contact transducers. The transducer diameter was approximately 5 mm. The transducers were orientated perpendicularly to the surface of the object to be measured and ultrasonic gel was applied as a coupling agent. The vertical and lateral position of each transducer could be adjusted manually and the axial position (scanning direction) using computer controlled stepper motors. The contact pressures between the transducers and the specimen were monitored using two precision load cells (Sensotec Model 31). During the scan, the transmitter was kept fixed and the receiver was moved away from the transmitter in steps (Fig 5.1). Typically the measurement was made at 40 transmitter to receiver distances r ranging from 20 to 50 mm corresponding to step size of 0.75mm. The receiving transducer was, in effect, dragged along the surface of the object to be measured with acoustic coupling maintained by the presence of ultrasonic gel and a near constant contact pressure. Lateral position was not adjusted during scans. The transmitter was excited by a square wave pulser (Panametrics 5077PR) yielding a signal bandwidth of 50 to 350 kHz (-20dB). The received signal was amplified and then digitised with a PC-based digital oscilloscope (National Instruments 5102) sampling at 10 MHz and averaging over, typically, 100 acquisitions. The received distance (r) - time (t) signal matrix was then visualised as a so-called (r,t) diagram (Fig 5.2), in which the intensity was represented conveniently using an absolute-valued grey scale.

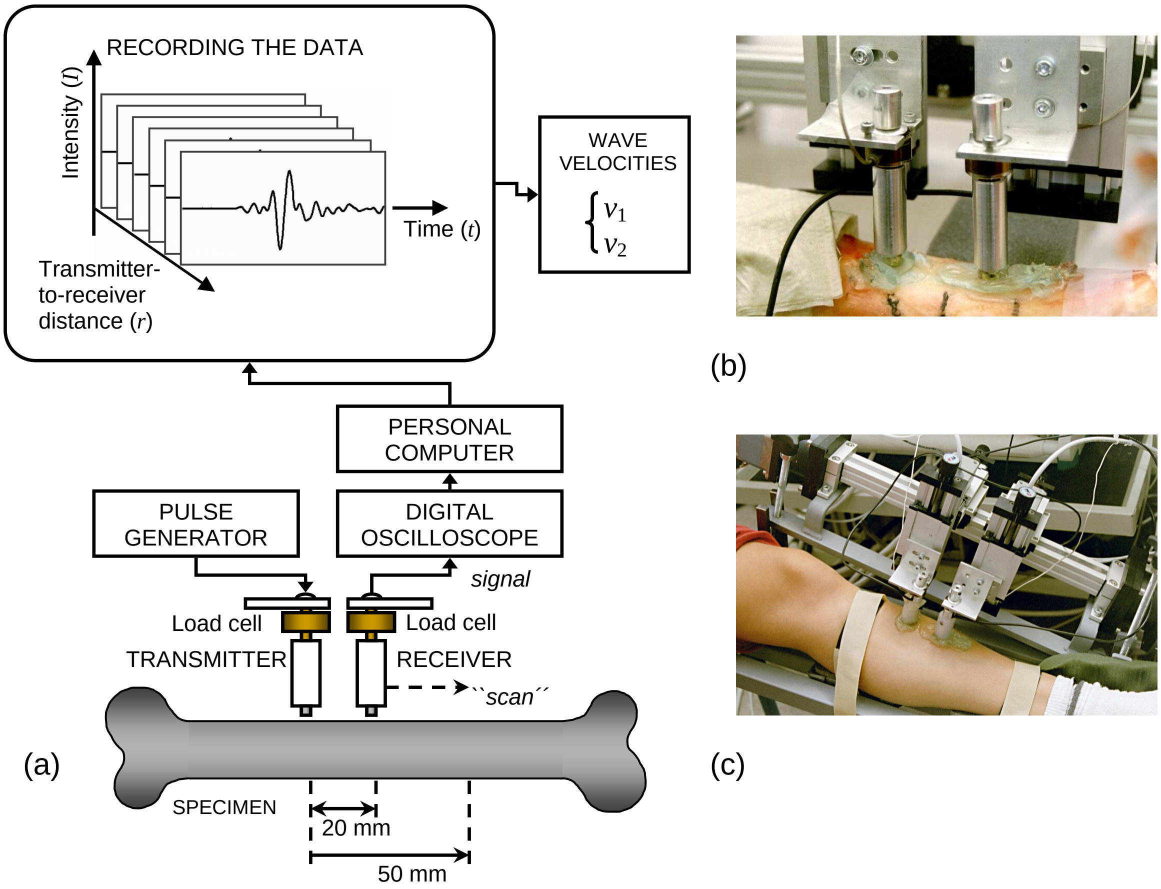

Fig. 5.1. a) Schematic diagram of the axial scanner device, and photographs of b) an in vitro and c) in vivo measurement.

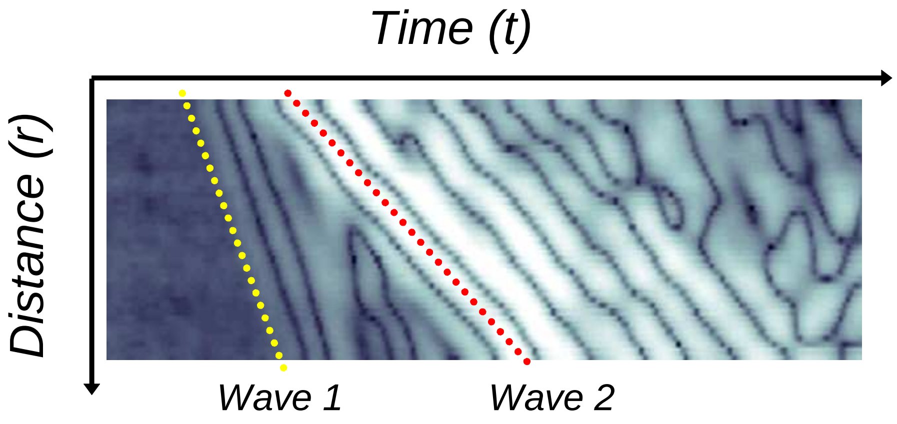

Fig. 5.2. A typical (*r*,*t*) diagram (human radius in vitro).

5.2 Methods of analysis

In the (r,t) diagrams two distinct wave modes were consistently observed (Fig. 5.2). The first of these (Wave 1) was a fast first arriving signal (FAS) and the second (Wave 2) was slower and corresponded to the fundamental antisymmetric Lamb mode (A0). The velocities of Wave 1 (v_1) and Wave 2 (v_2) were determined in the distance-time plane. In addition, two-dimensional spectral analysis was used for a more precise determination of v_2.

5.2.1 Distance-time analysis

Determination of the velocity in the distance-time plane consisted of two phases, a) detection of the time-of-flights t_i at the given distances r_i and b) linear regression in the detected points (r_i,t_i). This approach eliminated the delay due to overlaying soft tissue as discussed in Chapter 3.

The time-of-flights corresponding to Wave 1 were determined using a 25% threshold of the amplitude of the first detectable peak (Fig 3.1). A robust linear regression based on the least median of squares was then used for determining the velocity. The reason for using the robust regression was that often some failure points were involved among the determined time-of-flights, and this robust regression, giving lower weights for these failure points, determined the velocity more reliably than the ordinary least-mean-of-squares algorithm.

Determining the time-of-flights for Wave 2 was considerably more difficult than for Wave 1, as Wave 2 was dispersive and interfered by other wave modes. Therefore, different approaches for analysing Wave 2 were developed. The time-of-flights were always determined according to the maxima of the corresponding wave front. Sometimes Wave 2 was strong enough and the time-of-flights could be read from the recorded raw (r,t) diagram. The (r,t) matrix could also be processed using strong band-pass filtering, which enabled the measurement of dispersion, i.e. to determine the velocity at specific frequencies. When Wave 2 was weak compared to interfering waves, then specific group-velocity filtering and spectrum analysis methods were needed for a proper determination of v_2.

Where v_1 or v_2 are given without indication of the corresponding frequency, the frequency range from f = 250 to 300 kHz was used for v_1 and that from f = 100 to 150 kHz for v_2.

5.2.2 Spectral analysis

Two-dimensional fast Fourier transform (2D-FFT) has been used by several researchers for analysing distance-time matrices similar to the ones measured with the described low-frequency axial ultrasound scanner [1, 93, 54]. The 2D-FFT method was developed specifically for analysing signals which consist of overlapping wave modes that cannot be separated in the time history of the signal. The FFT separates such wave modes in terms of frequency and wavenumber. In the wavenumber-frequency plane the intensity maxima correspond to propagating wave modes, and if guided waves propagate, the locations of these intensity maxima are supposed to correspond to trajectories of guided waves (Fig. 5.3). Thus, the two-dimensional spectral analysis allows direct comparison between experimental results and theory. Moreover, determination of the velocities and dispersion of the identified wave modes is as well possible.

The 2D-FFT was based on the two-dimensional Fourier transform, as given by [1]

$$V(k,f)=\int_{-\infty}^{+\infty}\int_{-\infty}^{+\infty}u(r,t)e^{-i(kr+\omega t)}drdt\,, \tag{5.1}$$

where

$$u(r,t)=A(\omega)e^{i(\omega t-kr-\theta)} \tag{5.2}$$

is the displacement on the surface of the structure (assuming that a harmonic wave is propagating), $A(\omega)$ is a frequency-dependent amplitude constant, $\omega = 2\pi f$ is the angular frequency, k is the wave number and θ the phase. The measured (r,t) matrix represented the displacement $u(r,t)$.

The 2D-FFT made for the (r,t) matrix was often expressed as functions of phase velocity and frequency. The transformation from wavenumber k to phase velocity c_p was made point-by-point as $c_p = 2\pi f / k$ (Ref. V) (Fig. 5.3).

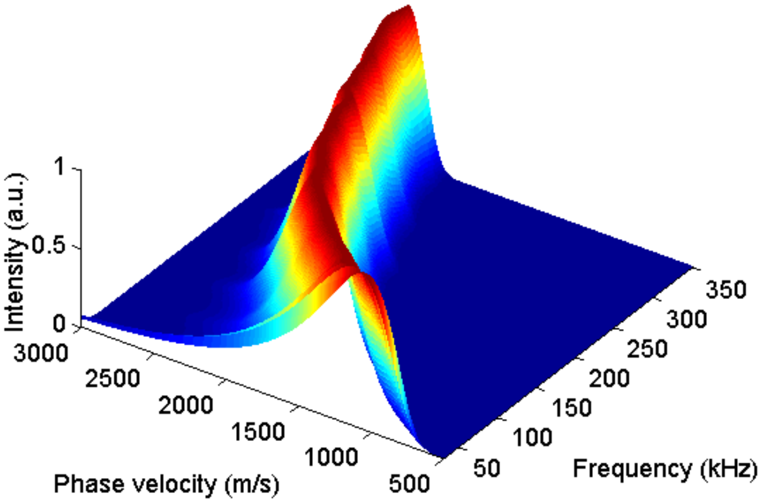

Fig. 5.3. 2D-FFT shows a ridge of intensity maxima that corresponds to a propagating wave mode. This result is for a free aluminium plate.

5.2.3 Inversion scheme

Inversion schemes have been used successfully for analysing guided wave data in different applications of non-destructive testing (e.g. Karim et al [44]) and also in one bone measurement study by Lefebvre et al [54]. The purpose of an inversion scheme is to determine one or more properties of the medium based on the measured guided wave ultrasound data. Karim et al introduced a method in which the dispersion equation of the given structure was minimised in terms of the elastic modulus in a large number of experimentally measured phase-velocity-frequency points. Lefebvre utilised this method using plate theory for axial transmission measurements of bovine bones, and determined estimations for the Young’s modulus. These approaches, however, require a broad-band multi-mode guided wave measurement.

We developed a fairly different approach because we, so far, only measured one genuine guided wave mode (A0) and a reliable identification of this mode required the use of selective time domain filtering. In addition, our essential interest here was to clarify how well the measured A0 Lamb mode could reflect the thickness of a plate or a cortical wall. Therefore we did not attempt to determine the Young’s modulus, as yet, but made the inversion in terms of thickness h with given material properties (e.g. c_L and c_T).

While the time-domain (or group-velocity) filtering included adjustable input parameters, the inversion scheme was actually considered as a theory based signal processing feedback loop (Fig. 5.4). The preliminary input parameters were material properties (e.g. c_L and c_T), thickness h and time delay t_d. The output parameters were (v_e^i, f_i), h and t_d, where v_e^i were the experimental phase velocities at corresponding frequencies f_i; and h and t_d the fitting parameters. The fitting was made by means of the minimisation

$$\min\left(\sum_{i=1}^{N}\left|v_e\left(f_i,t_d\right)-c_p\left(f_i,h\right)\right|\right), \tag{5.3}$$

where $c_p(f_i,h)$ were the computed theoretical phase velocities. The approach can be applied either using an assumed constant c_g value or allowing to c_g to vary as a function of frequency. In general, a constant c_g value was used. The constant c_g was typically determined according to the average or maximum level of the corresponding group velocity curve.

Our inversion scheme was thus tightly connected with the identification of an experimental wave mode, yielding more reliable phase-velocity trajectory (v_e^i, f_i) than the 2D-FFT alone. Therefore we called this process also as the selective 2D-FFT (Ref. V).

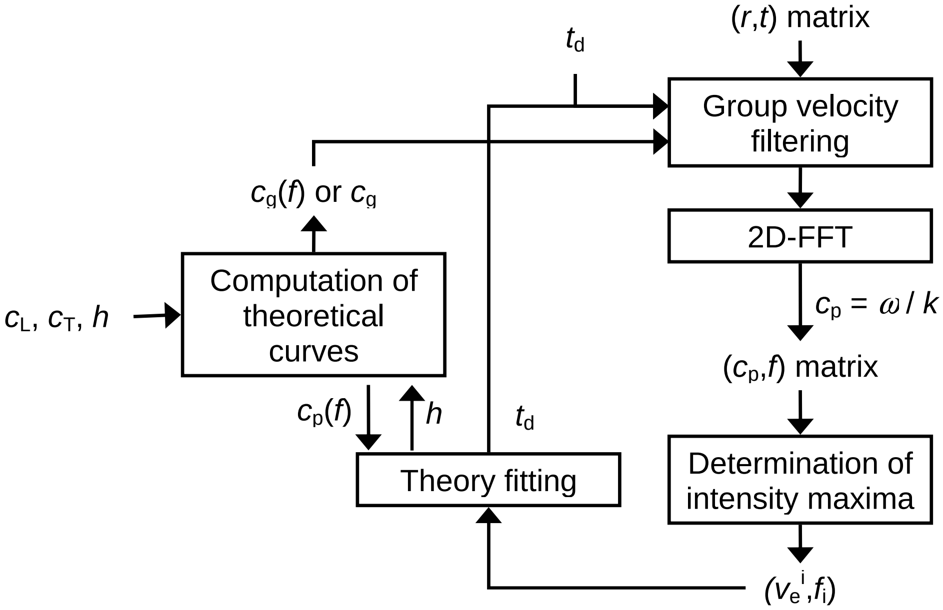

Fig. 5. 4. Principle of the inversion scheme and signal processing feed back loop.

5.3 Finite-element simulation

Analytical modelling of guided waves is possible only in simple uniform sample geometries, such as plates and tubes. Thus the effect of some relevant bone properties, such as a non-symmetrical shape, porosity and defects, must be modelled using numerical simulation of wave propagation. The methods of numerical modelling date back to the 1940’s, though the more active interest in the utilisation of these methods has arisen together with the rapid development of computers after the 1960’s [113]. There are two principal approaches of numerical modelling, finite-difference and finite-element method (FEM) [1, 24]. Since then, it has been shown that FEM is more effective and accurate in terms of modelling guided waves, as the free boundaries are better accommodated with this method [1, 66, 93]. Also, the axial propagation of the lateral wave in cortical bone has been modelled using a two-dimensional [11, 72] (Ref. I) and three-dimensional finite-difference method [12]. In contrast with some previous results, the finite-difference method (more specifically the so-called Virieux difference method) was found as to be the most accurate approach for simulating the fluid-solid interaction in immersed bone samples [12]. However, it must be noted that comparison of these two approaches is not as simple, as plenty of different modifications of the finite-difference and finite-element method have been developed for the needs of various applications [24].

Several commercial general-purpose programs are available for numerical modelling, such as ABAQUS/Explicit (ABAQUS Inc., Warwick, Rhode Island, USA) [93], and Wave2000 Pro (CyberLogic Inc., New York, USA). Sometimes these programs may, however, lack features that are required for specific wave propagation problems. It may thus be more flexible to use a custom made, specialised wave propagation code.

Our purpose was to simulate the low-frequency ultrasonic guided wave measurements in simple two- and three-dimensional structures in order to validate the measurement principle against analytical theory, and to model the properties of bone that affect the measurement but are not possible to model analytically. We started the simulations using Wave2000 Pro (Ref. I), based on the finite difference method, but encountered some difficulties in observing guided waves. Therefore, we began to seek custom-made software to handle the two-dimensional simulation of guided waves in a traction-free isotropic plate. This software was developed in collaboration with our group by Erkki Heikkola in a related AKTINUM-project at VTT Processes (Jyväskylä, Finland) and Numerola Oy (Jyväskylä, Finland).

The finite-element method was used to simulate the vibration of an isotropic plate. The plate, denoted by Ω, is assumed to be homogeneous and to have uniform thickness *h* (see Fig. 5.5). Simulations were based on the two-dimensional linear elasticity equation with the plane strain assumption. In this case, the displacement $\vec{u} = (u_1 \; u_2)^T$ is governed by the system of equations

$$\rho \frac{\partial^2 \vec{u}}{\partial t^2} - \mu \Delta \vec{u} - (\lambda + \mu) \nabla (\nabla \cdot \vec{u}) = 0, \tag{5.4}$$

where λ and μ are the Lamé constants and ρ the density of the material. These parameters are connected to the pressure and shear (longitudinal and transverse) wave velocities such that

$$c_L = \sqrt{\frac{\lambda + 2\mu}{\rho}}, \quad c_T = \sqrt{\frac{\mu}{\rho}}. \tag{5.5}$$

The stress tensor $\tau(\vec{u})$ of the elastic medium is given by

$$\tau_{ij} = \lambda \delta_{ij} (\varepsilon_{11} + \varepsilon_{22}) + 2\mu \varepsilon_{ij}, \quad i, j = 1,2, \tag{5.6}$$

where δ_{ij} is the Kronecker symbol and ε_{ij} is the linear strain tensor,

$$\delta_{ij} = \begin{cases} 1, & i = j, \\ 0, & i \neq j, \end{cases} \quad \varepsilon_{ij} = \frac{1}{2}\left(\frac{\partial u_i}{\partial x_j} + \frac{\partial u_j}{\partial x_i} \right). \tag{5.7}$$

The condition on the boundaries of the plate is of the form $\tau(\vec{u})\vec{n} = \vec{g}$, where $\vec{n}$ is the outward unit normal to the boundary. The right-hand side of the boundary condition is zero on all other boundaries except the transducer interface Γ_t. This case corresponds to the interface of a solid with air. On the transducer interface the second component of vector $\vec{g}$ is a time-dependent signal corresponding to vibration of the transducer in the direction perpendicular to the plate. This signal initiates the vibration of the plate, and the frequency band of the signal is bounded to the interval 100-300 kHz.

The signal in the receiver at time *t* is measured by computing the following integral over the receiver interface Γ_r:

$$\int_{\Gamma_r} \left| \vec{u}(t) \cdot \vec{n} \right|^2 ds. \tag{5.8}$$

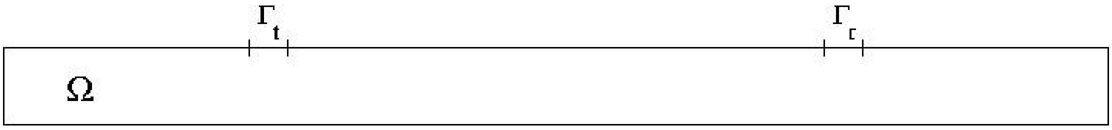

Fig. 5.5. The plate and locations of the transducer and the receiver.

Attenuation of the vibration is modelled by adding mass proportional damping to Eq. (5.4). This assumption leads to the system of equations

$$\rho \frac{\partial^2 \vec{u}}{\partial t^2} + 2\alpha\rho \frac{\partial \vec{u}}{\partial t} - \mu \Delta \vec{u} - (\lambda + \mu)\nabla(\nabla \cdot \vec{u}) = 0, \tag{5.9}$$

where the attenuation parameter $\alpha > 0$ determines the rate of decay with respect to mass and velocity deformation.

The finite-element method requires the following formulation of the elasticity equation. Find the displacement field $\vec{u}$ such that

$$\int_{\Omega} \rho \frac{\partial^2 \vec{u}}{\partial t^2} \cdot \vec{v}\, dx + 2\alpha \int_{\Omega} \rho \frac{\partial \vec{u}}{\partial t} \cdot \vec{v}\, dx + \int_{\Omega} \tau(\vec{u}) : \varepsilon(\vec{v})\, dx = \int_{\Gamma_t} \vec{g} \cdot \vec{v}\, ds \tag{5.10}$$

for all displacement fields $\vec{v}$. This equation holds at all times t, and time-dependent simulation is started from the initial conditions $\vec{u}(0) = 0$ and $\frac{\partial \vec{u}(0)}{\partial t} = 0$.

Spatial discretisation with the finite-element method requires a triangular mesh for the plate. The number of nodes in the mesh is denoted by N. Discretisation leads to the semi-discrete equations of motion

$$M \frac{\partial^2 U}{\partial t^2} + 2\alpha M \frac{\partial U}{\partial t} + K U = G, \tag{5.11}$$

where the $2N \times 2N$ -matrices M and K are the finite-element mass and stiffness matrices. The vector G corresponds to the source signal $\vec{g}$ and vector U contains the nodal values of the displacement components.

The standard central-difference method is used to discretise the equation with respect to time. If we denote the discretisation time step by Δt, and the solution U at time $t_i = i\Delta t$ by U_i, then the equation for computing the solution U_{i+1} from the two previous time steps is given by

$$(1 + \Delta t\, \alpha) M U_{i+1} = M(2U_i - U_{i-1}) + \Delta t \alpha M U_{i-1} - \Delta t^2 K U_i + \Delta t^2\, G_i. \tag{5.12}$$

Each time step involves the solution of this linear system, which is obtained by Cholesky factorisation of the mass matrix M. The central-difference method is second-order accurate with respect to time, but it is only conditionally stable. In other words, the time step Δt needs to be smaller than a given threshold depending on the finite-element mesh density and the wave velocity. If the mesh is refined, also the time step needs to be reduced to keep the time iteration stable.

Chapter 6

Results

6.1 Validation of the measurement principle (2D simulations for plates)

A two-dimensional finite element approach was used to simulate wave propagation in a free plate. Source and receiver geometry corresponded to that of the experimental axial transmission system, and the frequency range of the short transmitted pulse was 50-350 kHz (-20 dB). The objective of these simulations was to investigate the nature of the propagating signals in the proposed low-frequency axial scanning method. More specifically, the aims were to measure the velocities of the wave modes present, assess their dispersion and relation to plate thickness, and to compare the simulated results to those expected for Lamb waves in plates.

Material properties corresponding approximately to those of an isotropic bone (Young's modulus E = 23.8 GPa, Poisson ratio ν = 0.3 and density ρ = 2.0 g/cm^3) were chosen as the simulation parameters. According to Eqs. (3.1) and (3.2), the corresponding bulk velocities were $c_L \cong 4000$ m/s and $c_T \cong 2140$ m/s.

Figure 6.1 shows (r,t) diagrams for simulations in plates with thickness ranging from 1.0 to 4.0 mm. The fast Wave 1 (First Arriving Signal or FAS) and a slower Wave 2 can be identified in all diagrams. Wave 1 had a lower intensity than that of Wave 2. The velocity v_1 of Wave 1 ranged from 3616 to 4006 m/s for thicknesses h = 1 - 10 mm, respectively (Fig 6.2). The mean frequency of Wave 1 was estimated roughly as 300 kHz by looking at the pulse lengths of the first arriving signal. Wave 2 was strongly dispersive in a thin plate, the higher frequency components arriving first and the lower frequency ones arriving later, considerably delayed. In a thick plate dispersion was much weaker, as expected. The velocity v_2 (100 kHz) ranged from 790 to 1800 m/s for h = 1 - 10 mm, respectively (Fig 6.2).

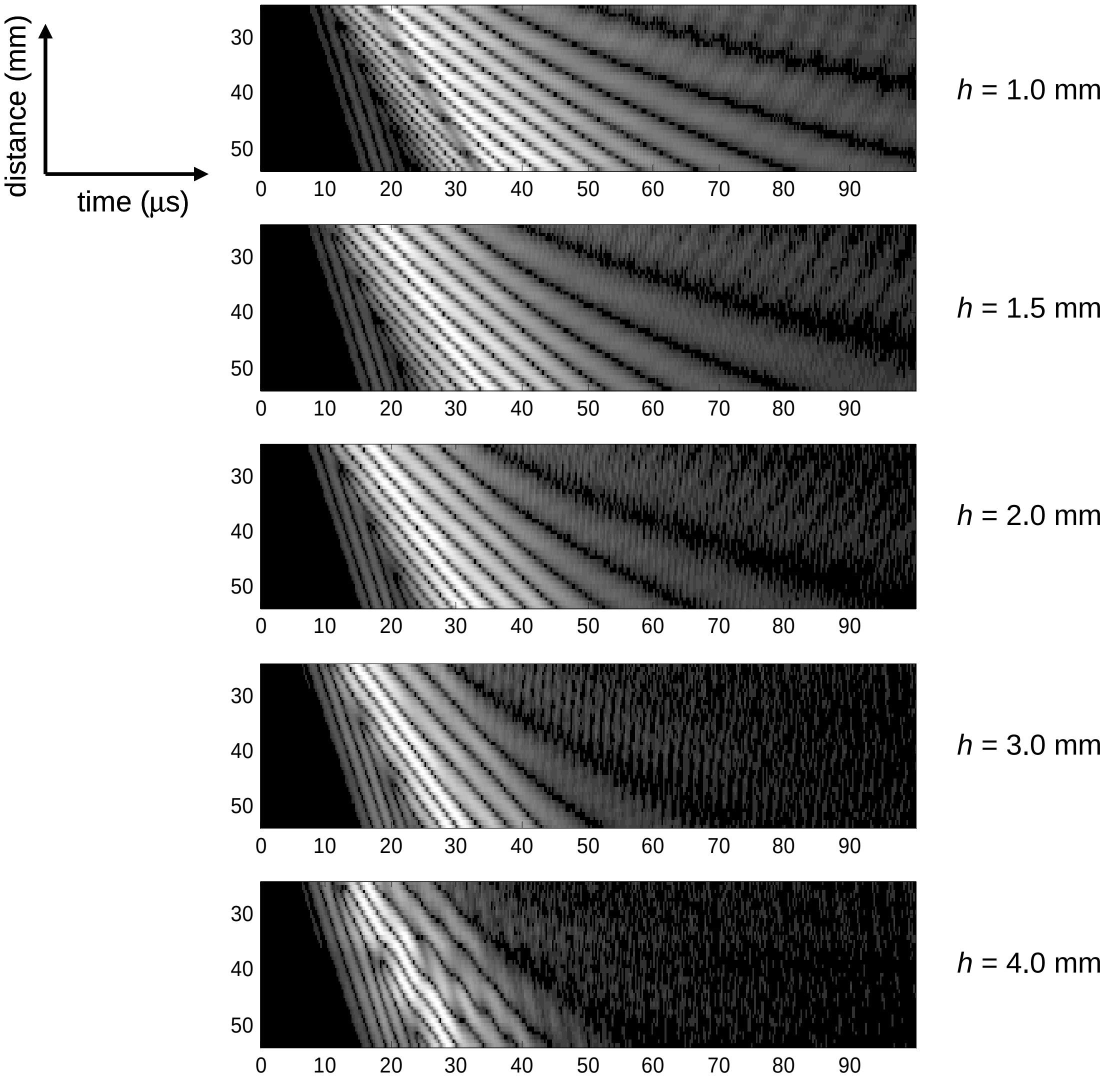

Fig. 6.1. Effect of plate thickness *h* on the wave modes seen in the (r,t) diagrams. FEM simulation results for plates with isotropic material distribution.

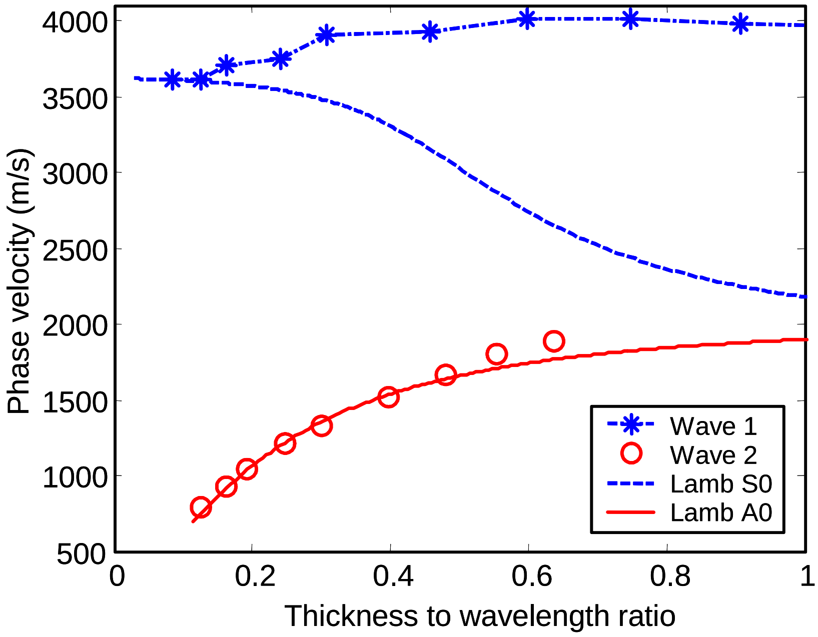

Fig. 6.2. FEM simulation results for the phase velocities of Wave 1, Wave 2 and fundamental Lamb modes as functions of the thickness to wavelength ratio.

Velocity v_1 was consistent with that of the lateral wave propagating at the bulk velocity when thickness to wavelength ratio (h/λ) was greater than 0.5. For $h/\lambda < 0.5$, v_1 decreased towards the phase velocity of an S0 Lamb mode. For a 1 mm plate $v_1 = 3616$ m/s, corresponding exactly to the saturation level $(f,h\rightarrow 0)$ $c_{S0} = (E/(\rho(1-\nu^2)))^{½} \cong 3616$ m/s of the S0 mode in the thin plate and low frequency limits [32]. Velocity v_2 was fairly consistent with the phase velocity of an A0 Lamb mode throughout the simulated thickness range.

Using 2D-FFT within the frequency range $f = 50$ - 350 kHz, clear intensity maxima curves were obtained (Fig 6.3). The intensity maxima $(v_2^{\mathrm{i}},f_{\mathrm{i}})$ (diamond markers) were in excellent agreement with the computed phase velocities of the A0 Lamb mode (solid lines, computed for the same material parameters and plate thickness as used in the simulation).

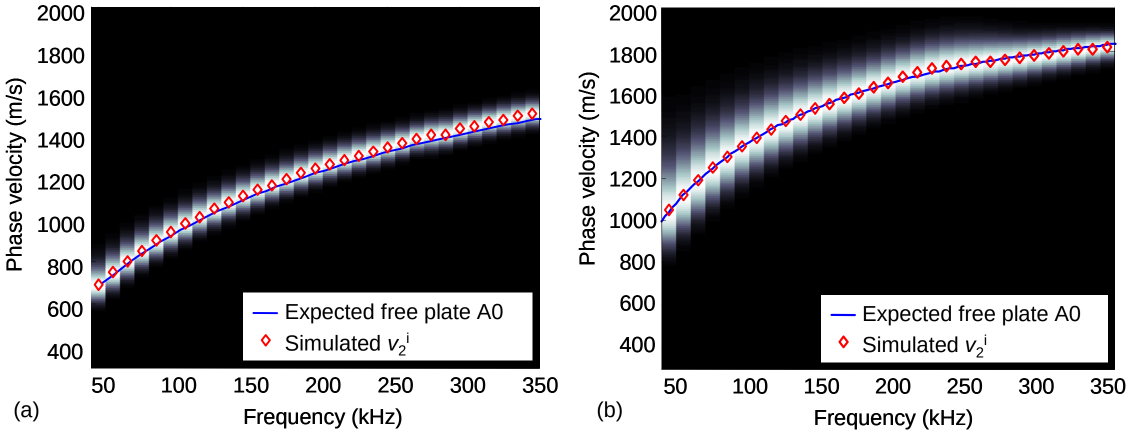

Fig. 6.3. The locus of the intensity maximum in the (v_e,f) plane for FEM simulations of isotropic bone plates with thicknesses of a) h = 1.5 mm and b) h = 4.0 mm.

6.2 Validation of the measurement system (results for plates)

The low frequency axial transmission device was used to measure a range of acrylic plates in order to confirm the presence of two propagating waves, and to assess the velocity of these waves as a function of frequency and plate thickness.

Perspex acrylic (c_L = 2730 m/s, c_T = 1325 m/s and ρ = 1.186 g/cm^3, corresponding to Young's modulus E = 5.60 GPa and Poisson ratio ν = 0.347) was chosen as the phantom material. Twelve plates with thicknesses ranging from 2 to 24 mm were measured. The plate thickness h was measured using a caliper. For each plate the ultrasound scan was repeated three times.

The (r,t) diagrams for the acrylic plates were similar to those for the numerical simulations. Two wave modes, Wave 1 and Wave 2, were observed consistently (Ref. I). Wave 1 (estimated f = 250 kHz) was consistent with the lateral wave in thick plates and it tended towards an S0 Lamb mode for $h/\lambda < 0.5$ (Fig 6.4, cross markers). Wave 2 (f = 100 kHz) was consistent with an A0 Lamb mode for $h/\lambda < 0.5$. However, in thick plates the observed v_2 was affected by the S0 as well as the A0 mode, and the results were not clear for $h/\lambda > 0.5$ if no selective filtering was used (Fig 6.4, dot markers). When using selective time domain filtering (or group-velocity filtering), v_2 as a function of frequency followed more precisely the dispersion curve of the A0 mode also for thick plates (Fig 6.4, circle markers).

When using the selective 2D-FFT and inversion scheme within the frequency range f = 30 - 350 kHz, clear intensity maxima (v_2^i,f_i) (diamond markers) were obtained for thin as well as for thicker plates (Fig 6.5). These experimental results were in a good agreement with the computed dispersion curves of A0 mode (solid lines).

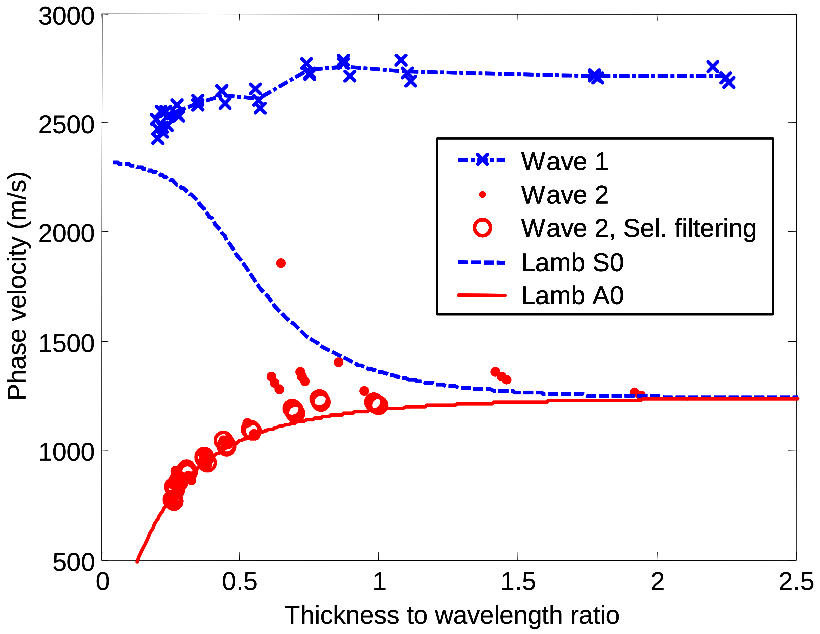

Fig. 6.4. Experimental results for acrylic plates. Velocities v_1, v_2, and phase velocity of fundamental Lamb modes are shown as functions of the thickness to wavelength ratio.

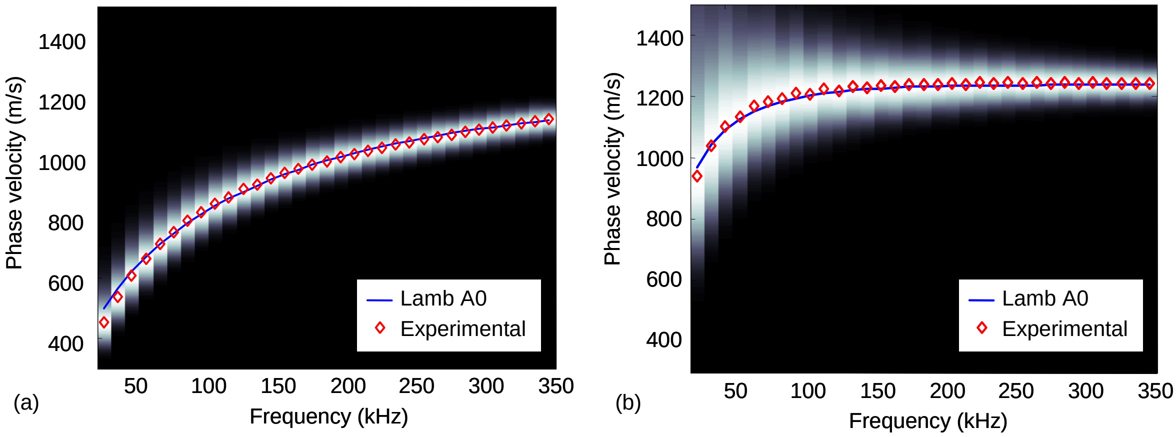

Fig. 6.5. The locus of the intensity maximum in the (v_e,f) plane as measured for acrylic plates with thicknesses of a) *h* = 2.2 mm, and b) *h* = 12 mm. Diamond markers denote the measured velocity of Wave 2 as determined from the intensity maxima (white) and the solid lines show the respective phase velocities of the plate A0 mode. Selective 2D-FFT was used.

The inversion scheme used yielded an estimate h_e for plate thickness, which was in excellent agreement with the true plate thickness *h* in the thickness range 2 to 8 mm (Ref. V). For thicker plates there is less dispersion in the phase velocity in the investigated frequency range, and therefore thickness estimation was not as accurate as for thin plates.

6.3 Effect of sample geometry (results for tubes)

The objectives of this study were to clarify how a tubular shape of the sample affects the measured velocities v_1 and v_2, and also how reliably the wall thickness of the tube can be estimated when using plate theory in the inversion scheme.

Acrylic was again used as the phantom material. Four hollow tubes with an outer radius of *b* = 10.0 mm and a wall thickness *e* ranging from 2.2 to 8.0 mm, were measured such that each ultrasound scan was repeated three times.

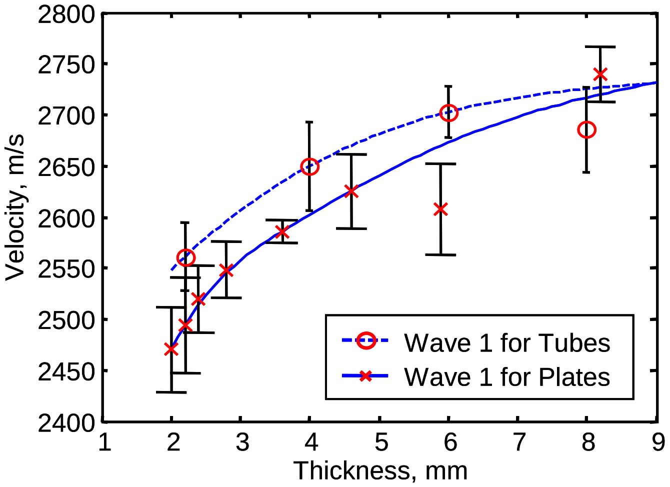

Fig. 6.6. The velocity of Wave 1 as measured for acrylic tubes and plates of varying thickness.

The velocity v_1 measured for tubes showed a similar dependence on wall thickness as that measured for plates (Fig 6.6). However, v_1 was about 4% higher for tubes than for plates when the thickness was less than 6 mm. When the thickness was 6 mm or greater, then the difference was not clear between the velocities for plates and tubes.

Dispersion curves for velocities v_2 were determined using a selective 2D-FFT assuming plate theory in the inversion scheme. When the tube-wall thickness e was small compared to the outer radius of the tube b, then the fundamental flexural tube mode (F11) was fairly consistent with the trajectory of the A0 plate mode in the investigated frequency range (Fig 6.7). Indeed, the experimental velocities (square markers) corresponded fairly well to those of F11 (or A0) when the tube wall was thin (e = 2.2mm). When thickness e increased with respect to b, then v_2 was higher than that of the A0 mode. Correspondingly, the phase velocity of F11 increased as well, being in satisfactory agreement with the experimental results.

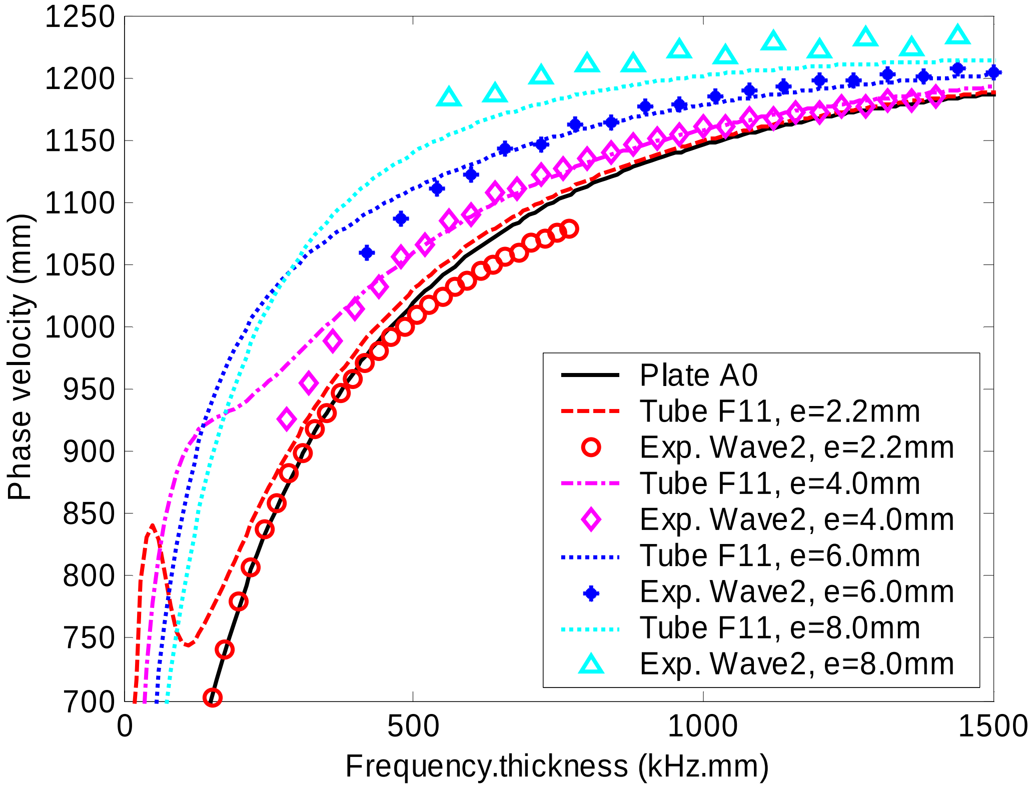

Fig. 6.7. Experimental velocities for Wave 2 as measured for hollow acrylic tubes, and the theoretical curves computed with the corresponding tube dimensions. Experimental velocities were determined using a selective 2D-FFT together with an inversion scheme based on plate theory.

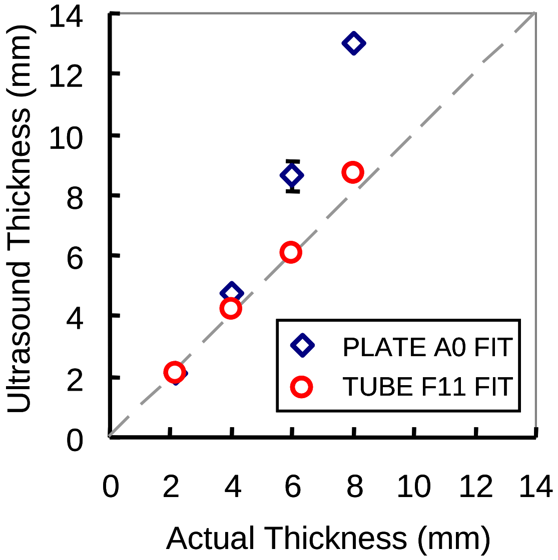

Fig. 6.8. Ultrasound thickness h_e versus the actual tube-wall thickness *e*. Ultrasound thicknesses were obtained by an inversion scheme using a) a plate A0 mode (diamond markers) and b) a tube F11 mode (circle markers) when fitting the results measured for acrylic tubes.

The inversion scheme used also provided wall-thickness estimates h_e (Fig 6.8). When using the plate model (A0 mode), the obtained thickness h_e was in good agreement with the actual wall thickness *e* only when *e*/*b* was small (*e* = 2.2 mm). For e > 2.2 mm, $h_e > e$, and the error between h_e and *e* increased with increasing ratio *e*/*b*, being 60% at *e* = 8mm. When using the tube model (F11 mode) and constant c_g, the wall-thickness estimate h_e agreed, with a difference of at most 10%, with the true thickness in the thickness range *e* = 2.2 - 6.0 mm, and with a 15% difference for e = 8.0 mm. Using variable c_g improved the precisions of h_e slightly. At this stage of method development the use of variable c_g in the inversion scheme has not been optimised, however.

6.4 Effect of irregular cross-section (results for anatomically shaped bone phantoms)

Measurements were made with the axial transmission device in phantoms with an anatomically realistic (non-spherical) cross-sectional shape in order to clarify how cross-sectional geometry affects the measured velocities v_1 and v_2, and the thickness estimate h_e (using plate theory).

Polyvinyl chloride (PVC, c_L = 2400 m/s, c_T = 1060 m/s and ρ = 1.4 g/cm^3) was chosen as the phantom material as it was easy to manufacture in an anatomical shape. One drawback of using PVC is that its longitudinal and shear velocities are substantially lower than those in bone, and this must be remembered when interpreting results from such phantoms. Two tubular bone phantoms had a circular central hole and an outer cross-sectional profile mimicking that of the human tibia. A ”thick” and ”thin” phantom were manufactured, having medullary canal diameters of 15 mm and 19 mm, respectively. The cross-sectional profiles of the two phantoms are shown in Fig. 1 of Ref. III. Ten measurement sites were marked around each phantom. At each measurement site, the thickness of the phantoms along a line normal to the surface of the inner circle was measured using a caliper (the mean value of three measurements). In the ”thick” phantom local thickness determined in this way varied from 5.2 to 13.3 mm, and in the ”thin” phantom it varied from 2.6 to 10.2 mm.

For PVC plates results corresponding to those obtained for acrylic plates were first measured for calibration purposes.

For anatomically shaped bone phantoms the dependence of v_1 on the local radial wall thickness was confirmed. As expected, v_1 decreased with the decreasing wall thickness (Figs. 2 and 3 of Ref. III). The measured v_1 was found to vary by 17.1% and 21.4% depending on the location of the measuring site around the ”thick” and “thin” phantom, respectively. Measured v_1 was strongly linearly correlated with the local thickness ($r^2 = 0.81$, $p<0.001$) (Fig. 3 of Ref. III).

Correspondingly, v_2 (at f=100kHz), as determined using the selective 2D-FFT and the inversion scheme (plate theory), correlated linearly with the local thickness ($r^2 = 0.76$, $p<0.001$). The value of v_2 (at f=100kHz) varied by 18.8% and 33.0% depending on the location of the measuring site around the ”thick” and “thin” phantom, respectively. The local wall thickness estimate h_e, obtained from the inversion scheme, correlated linearly with the actual local wall thickness h ($r^2 = 0.78$, $p<0.001$), though h_e was 30% lower than h ($p<0.001$) (Fig. 6.9). The trend of this difference is contradictory with the expected difference between the plate and tube models (Figs. 6.7, 6.8), and the explanation remains, as yet, inconclusive.

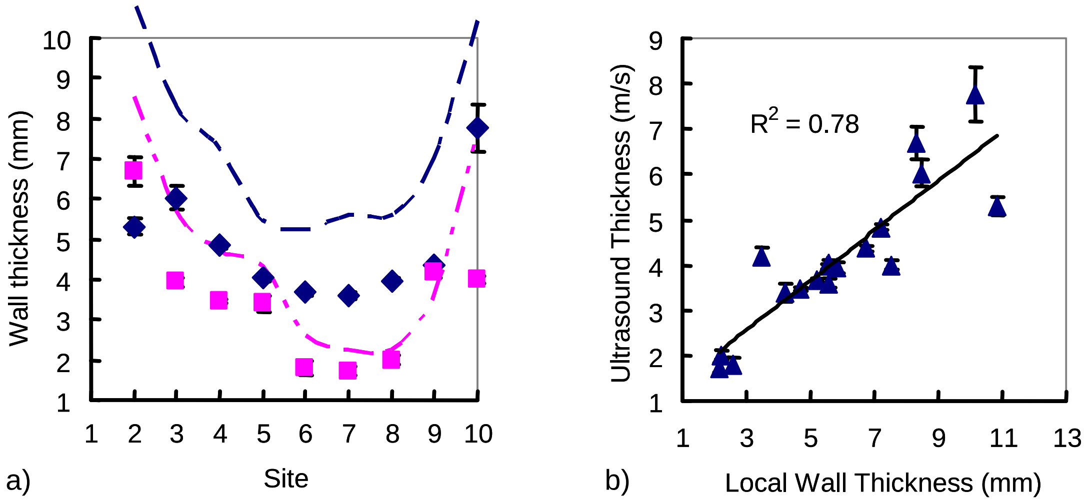

Fig. 6.9. a) Wall thickness estimates h_e for the “thick” (diamond markers) and “thin” (square markers) anatomically shaped bone phantom as a function of measurement site. Corresponding local thicknesses h are shown by dashed lines. b) Correlation between the ultrasound thickness h_e and local wall thickness h (results for two phantoms).

6.5 Effect of overlying soft tissue (results for immersed plates)

Immersed plate was measured using the axial transmission device in order to test if immersion affects the reliability of measuring Wave 1, to test if plate model yields a satisfactory interpretation of Wave 2 in this case, and to evaluate the usefulness of the fluid-solid bilayer model so as to provide an improved interpretation of Wave 2.

Aluminium plate (h = 4.0 mm, c_L = 5950 m/s, c_T = 3120 m/s and ρ = 2.7 g/cm^3, corresponding to Young's modulus E = 68.9 GPa and Poisson ratio ν = 0.31) was chosen as the bone phantom and water (c_F = 1500 m/s) on top of the plate played the role of soft tissue. All measurements were made underwater, in varying immersion depths of 0 to 12 mm. The thickness of the thin overlying water layer was carefully adjusted according to the area of the water tank and the volume of the new water added. Transducers were hold on top of the water, and their vertical position was controlled within 0.1 mm.

The velocity of Wave 1 was v_1 = 5383 (cv = 2.5%) for immersion depths $a \leq 8$ mm (Fig. 6.10). For a > 8 mm, a reliable determination of v_1 was not possible. For a dry aluminium plate v_1 = 5533 (cv = 1.2%). The mean error when measuring v_1 for an immersed plate was thus -2.7%. The thickness to wavelength ratio was h/λ = 4.0 mm · 300 kHz / 5500 m/s = 0.22, thus v_1 can be assumed to be lower than c_L = 5950 m/s and slightly greater than c_{S0} $(h,f\rightarrow 0) = (E/(\rho(1-\nu^2)))^{½} \cong 5313$ m/s [32].

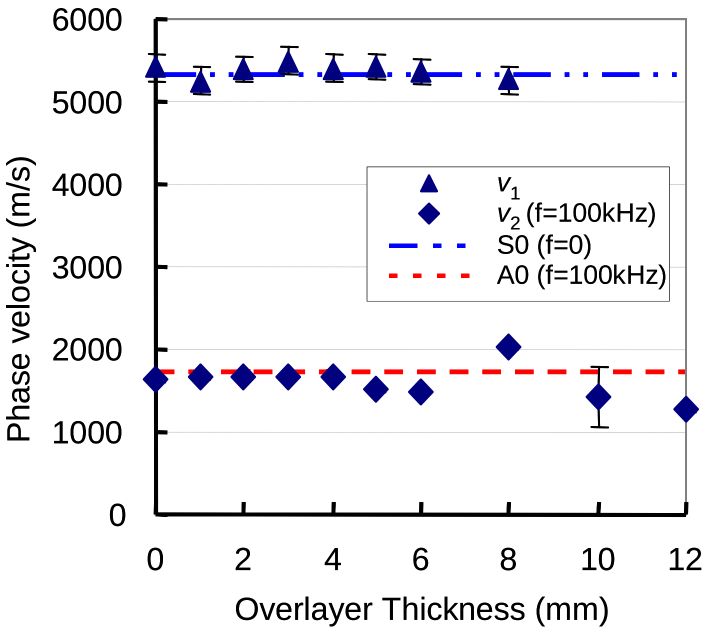

Fig. 6.10. Velocities v_1 (triangle) and v_2 (diamond) as functions of overlayer thickness. The velocities of the S0 and A0 Lamb modes, computed for similar plates, are shown for comparison.

From Eq. (3.12) we recall that the overlayer must be thinner than $a_{\mathrm{max}} = r_{\mathrm{min}}\,[1-(c_{\mathrm{F}}/v_1)^2]^{\frac{1}{2}}\,[2(1+(c_{\mathrm{F}}/v_1))]^{-1}$, where c_{F} is the sound velocity in the fluid overlayer and v_1 the signal velocity in solid. When r_{min} = 20 mm, v_1 = 5500 m/s and c_{F} = 1500 m/s, then a_{max} = 7.6 mm. In practice, however, v_1 should be determined correctly if it is identified as the first arriving signal at least within 2/3 of the scanning range ($r_{2/3}$ = 30-50 mm). Thus r_{min} = 30 mm yields a_{max} = 11 mm.

It was not possible to measure v_2 reliably through a thin overlayer using the distance-time analysis or ordinary 2D-FFT. Only the use of the selective 2D-FFT approach yielded a satisfactory identification for Wave 2 (Ref. V). Using plate theory and constant c_{g} in the inversion scheme, the 2D-FFT yielded the mean velocity v_2 = 1600 m/s (*cv* = 14 %), at *f* = 100 kHz for *a* = 0 - 12 mm. For *a* = 0 - 4 mm, v_2 = 1663 m/s (*cv* = 1.5 %). For a dry plate v_2 = 1705 m/s (*cv* = 1.0 %) and the computed phase velocity (*f*=100kHz) is c_{A0} = 1719 m/s.

The inversion scheme (plate theory) yielded a satisfactory estimate h_{e} of the plate thickness for up to *a* = 6mm. For larger immersion depths *a*, the plate thickness could not be determined using plate theory in the inversion scheme (Ref. V).

The selective 2D-FFT approach was also tested using the first wave mode (BL1) of the water-solid bilayer model. BL1 required the use of a variable $c_{\mathrm{g}}(f)$ as the group velocity changed considerably at the investigated frequencies and thicknesses. The plate (*h* = 4mm) was measured for immersion depths of *a* = 1, 3, and 5 mm, and for parameters *a* and *h* their known values were used in the selective 2D-FFT. Doing so, the experimental dispersion curves for v_2 were qualitatively consistent with those of BL1 calculated using the corresponding values of *a* and *h* (Fig 6.11). Use of bilayer theory in the inversion scheme (i.e. in the determination of h_{e}) is not possible yet, but will soon become possible.

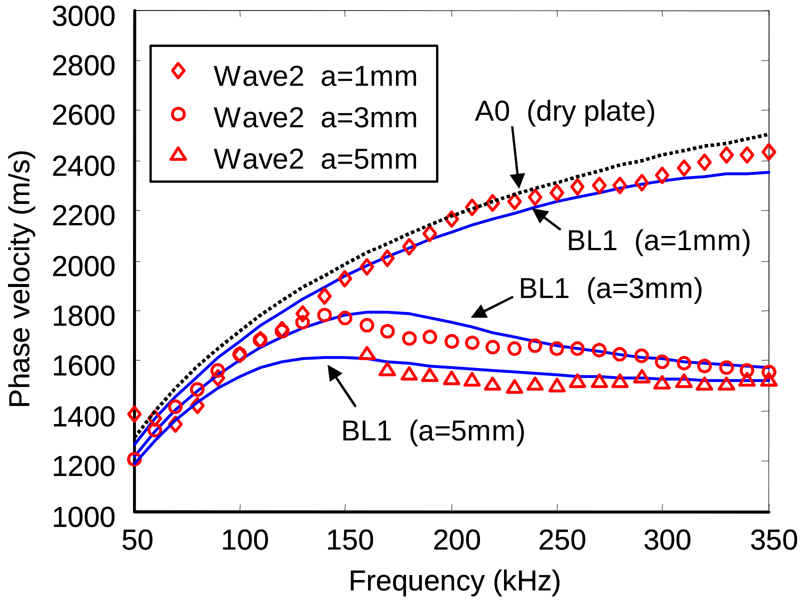

Fig. 6.11. Velocities of Wave 2 (markers) as determined using the selective 2D-FFT and variable c_{g} when analysing the results for a 4mm aluminium plate immersed at depths of 1, 3 and 5 mm. Parameters *a* and *h* had their known values. The results computed for the bilayer mode 1 (BL1, solid lines) at the same depths *a*, and the plate A0 mode (dashed line) are shown for comparison.

6.6 Application to real bone (in vitro)

Human radius specimens were measured using three different ultrasonic devices. The objectives were to show that Wave 1 (FAS) and Wave 2 (A0 guided wave) can be measured also in an actual bone, that the theory for plates can satisfactorily be used in the interpretation of the guided wave results, and that the theory for tubes can improve the interpretation. Another purpose was to verify that the two ultrasound velocities measured reflect bone quantities, such as bone mineral density (BMD) and cortical thickness (cTh).

In vitro measurements were made in collaboration with the Laboratoire d'Imagerie Paramétrique, Université Paris 6. Forty one (n=41) fresh human radius specimens were measured at the lateral mid-shaft (45% from the distal end). Three repeated measurements per specimen were made. The radius specimens were, in addition, measured with two other axial ultrasonometers, Omnisense (Sunlight Medical Ltd., Tel Aviv, Israel), and a bidirectional axial ultrasonometer prototype (Laboratoire d'Imagerie Paramétrique, Université Paris 6, Paris, France). Both of these devices operated at around 1 MHz frequency, being considerably higher than those used in our low-frequency axial scanner. The actual values of bone mineral density (BMD) and cortical thickness (cTh) were assessed using peripheral quantitative computed tomography (pQCT) (Norland/Stratec XCT 2000, Stratec Medizintechnik, Pforzheim, Germany).

The low-frequency Wave 1 (v_1 = 3799 m/s ± 179 m/s) and Wave 2 (v_2 = 1280 m/s ± 142 m/s) were both significantly slower than the FAS measured with the 1 MHz axial ultrasonometers ($p < 0.001$). Velocities v_1 and v_2 correlated significantly with cortical BMD (r=0.40, p<0.01; r=0.67, p<0.001, respectively) and cTh (r=0.33, p<0.05; r=0.72, p<0.001, respectively) (Table 3 of Ref. IV). The speed of sound (SOS) measured with the French prototype device yielded a relatively high correlation with cortical BMD (r=0.72, p<0.001) and also a weak correlation with cTh (r=0.36, p<0.05), whereas that of the Omnisense only correlated with the cortical BMD (r=0.50, p<0.001). In multivariate regression models (step-wise) v_2 was determined best by the combination of cTh and cortical BMD (r^2 = 0.62, p<0.001), or trabecular BMD and cortical BMD (r^2 = 0.62, p<0.001). However, all of the FAS velocities (including the low-frequency and both of the 1 MHz devices) were best determined by the cortical BMD alone. These results are described in detail in Ref. IV (note the difference in the notations of velocities).

The low-frequency measurements were also analysed using the inversion scheme and spectral analysis approach. The theoretical tube and plate models were used with c_L = 4000 m/s, c_T = 1800 m/s and ρ = 2.0 g/cm^3. In the tube model the outer radius b was approximated using the mean radius based on the total cross-sectional area measured by pQCT, yielding b = 6.28 mm ± 0.71 mm. The corresponding wall thickness was e = cTh = 2.53 mm ± 0.50 mm, and the thickness-to-radius ratio was e/b = 0.40 ± 0.07. From the latter it can be seen that the radius bones are quite strongly tubular, justifying the need for using the tube model (see Fig 6.7).

The thickness estimate obtained from the inversion scheme, when using the tube model, was h_e = 2.53 mm ± 0.67 mm, and it yielded a relatively high correlation with cTh (r=0.71, p<0.001) (Fig 6.12). In comparison, when using the plate model in the inversion scheme, the thickness estimate (h_e = 4.2 mm ± 1.8 mm) did not correspond well to the actual cTh, but correlation with cTh (r=0.67, p<0.001) remained as significant.

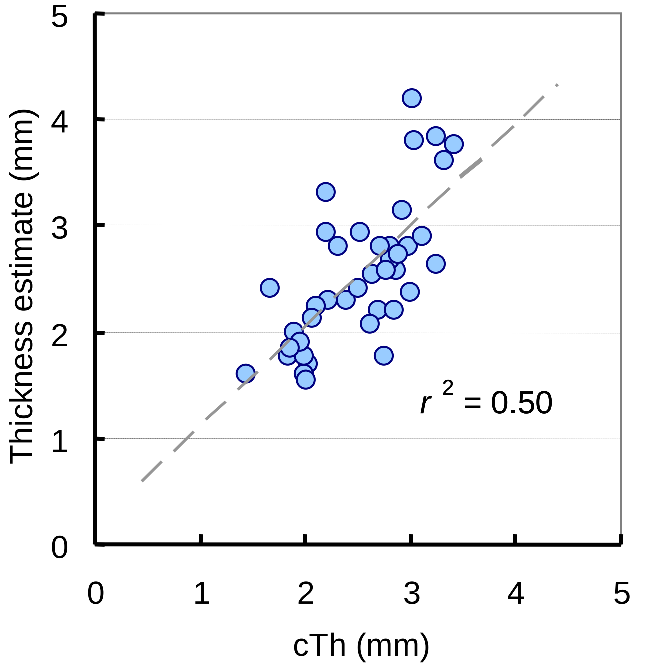

Fig. 6.12. The thickness estimate h_e (using tube model) versus actual cortical thickness *cTh*.

6.7 The clinical application (in vivo)

Human tibia was measured using the low-frequency axial scanner and one commercially available axial ultrasonometer (Omnisense, Sunlight Medical Ltd., Tel Aviv, Israel). The objective was to demonstrate that Wave 1 and Wave 2 can also be measured in vivo, reflecting the aspects of bone properties. Bone mineral density (BMD) and cortical bone thickness (cTh) were assessed using peripheral quantitative computed tomography (pQCT) (Norland/Stratec XCT 2000, Stratec Medizintechnik, Pforzheim, Germany) in the same site where the ultrasound measurements were made.

Two in vivo studies were made. In a small pilot study eight healthy normal and eight osteoporotic female volunteers were measured (Ref. I). The osteoporotic group had axial bone mineral density values, as measured using dual-energy x-ray absorptiometry, more than two standard deviations below the normal group. A more extensive study was made in a hundred and six 12-14-year-old girls (Ref. II).

The velocities of Wave 1 and Wave 2 were lower in the osteoporotic group (OP) than in healthy normal group (N) (Fig 6.13). However, a significant difference between these two groups was only obtained for Wave 2. In comparison, neither the speed of sound (SOS) nor cortical BMD discriminated significantly between the two groups.

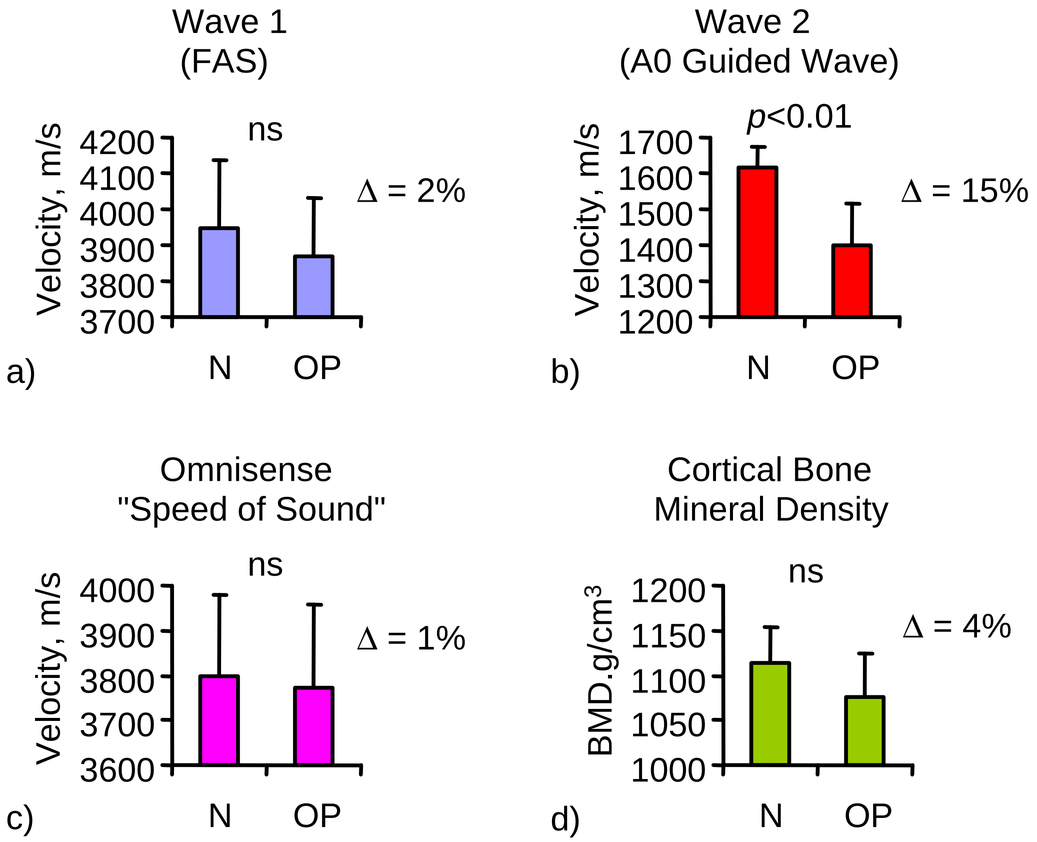

Fig. 6.13. Pilot in vivo results in the tibia of eight osteoporotic (OP) and eight healthy normal (N) female volunteers (Ref. I).

Table 6.1. Pearson's correlations between ultrasound and pQCT variables for the tibia of a hundred and six pubertal girls (Ref. II).

	v_1	v_2	$\mathrm{SOS}_{\mathrm{tibia}}$	**BUA**
cTh	.24 *	.28 **	ns	.43 ***
cBMD	.47 ***	.46 ***	.58 ***	.30 **
v_1		.57 ***	.33 **	.24 *
v_2			.23 *	.25 *

* p<0.05; ** p<0.01; *** p< 0.001

In the pubertal girls the velocities of Wave 1 and Wave 2 were v_1 = 3713 (182) m/s and v_2 = 1720 (92) m/s. Velocity v_1 correlated significantly with v_2 (r=0.57, p<0.001), and both of these velocities correlated weakly but significantly with SOS. Velocities v_1 and v_2 correlated significantly with cortical BMD ($r = 0.47$, $p < 0.001$ and $r = 0.46$, $p < 0.001$, respectively) and weakly but significantly with cTh ($r = 0.24$, $p < 0.05$ and $r = 0.28$, $p < 0.01$, respectively) (Table 6.1) (Ref. II).

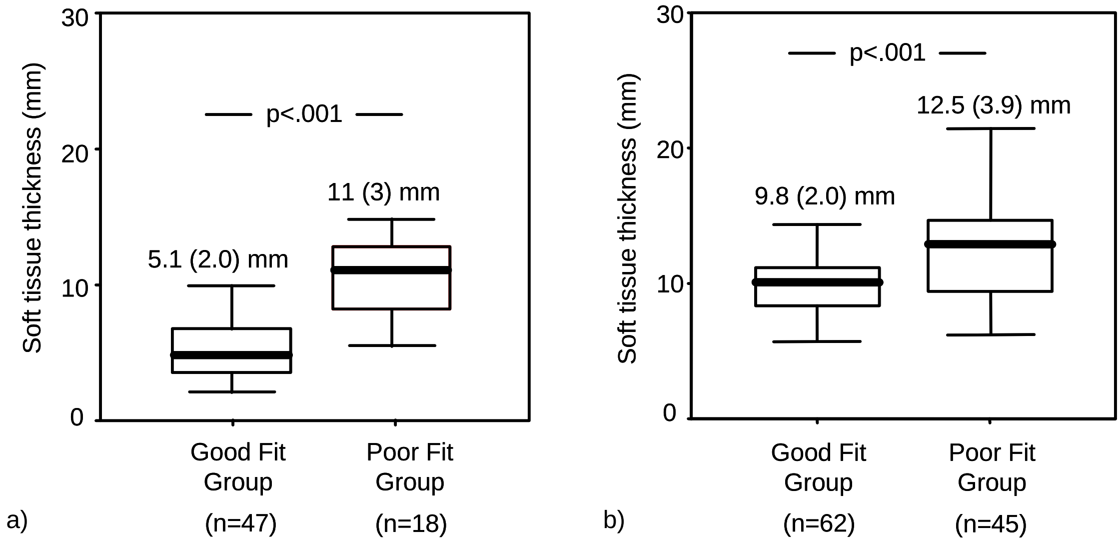

Fig. 6.14. Soft tissue thickness for the good and poor fit groups for a) tibia and b) radius. The quality of fitting was based on the visual judgement of how clearly the Wave 2 was seen in the (*r*,*t*) diagrams and how well the slope of the fitted line thus was expected to correspond to the velocity of A0 plate mode.

Two further in vivo studies were performed in Caucasian females, one for the tibia (age 32-90 years, n=65) and one for the radius (age 22-83 years, n=107). However, we encountered difficulties in measuring Wave 2 reliably at least in 1/3 of the subjects measured for the tibia and in 2/5 in those for the radius. The difficulties were identified as a consequence of too thick soft tissue on top of the bone (Fig 6.14). In the tibia the local soft tissue thickness (as measured using the pQCT at the site where the ultrasound measurements were made) ranged from 4 to 14 mm (±1 s.d.) between the subjects, and in the radius from 7 mm to 15 mm (±1 s.d.). As the soft tissue was thicker on top of the radius, this partly explains why the measurements were also more difficult for the radius than for the tibia.

Due to these difficulties in measuring through the soft tissue, we began an extensive program for explaining the effect of soft tissue theoretically and to develop more efficient analysis methods in order to eliminate the adverse effect of soft tissue. As yet, we have tested the plate model (A0 mode) with the inversion scheme and selective spectral analysis method for the improved determination of v_2 for the radius in vivo. This method enabled an automatic determination of the reliability of guided wave measurement based on the quality of the curve fit according to Eq. (10) of Ref. V. As a result, the in vivo radius data was divided, again, as a good fit (small fitting error between plate A0 mode and v_2, n=45) and poor fit group (large fitting error between plate A0 mode and v_2, n=62). Indeed, the soft tissue was thinner for the good fit (9.9 mm ± 3.1 mm) than for the poor fit (11.7mm ± 3.1 mm) sub-set of the radius data ($p<0.01$).

In the good fit group (n=45), velocity v_2 (as defined using the selective 2D-FFT and plate model) correlated significantly with the cortical BMD as well as cTh (Fig 6.15). No correlations between v_2 and the bone quantities were found for the poor fit group (n=62), but instead, v_2 yielded a strong correlation with the local soft tissue thickness (Fig 6.16).

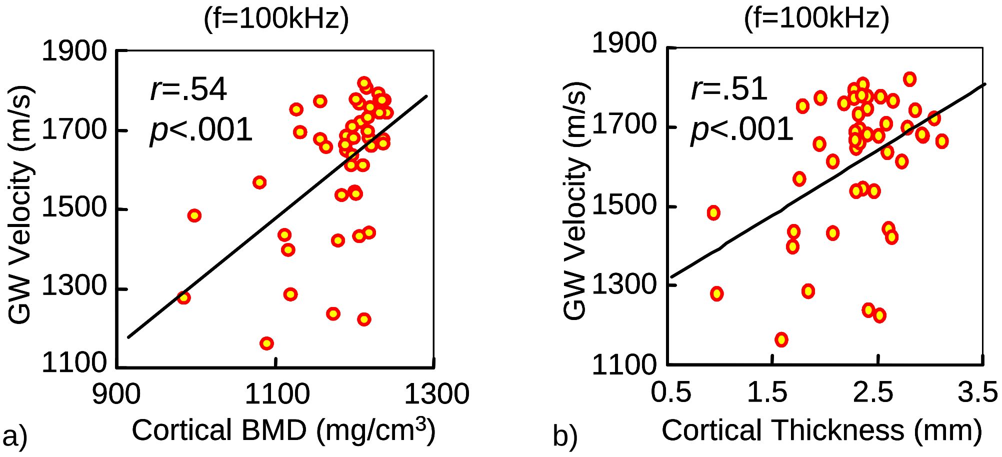

Fig. 6.15. Guided wave velocity v_2 (as determined using the selective spectral analysis and plate theory for the good plate theory fit group) versus bone quantities for the radius in vivo.

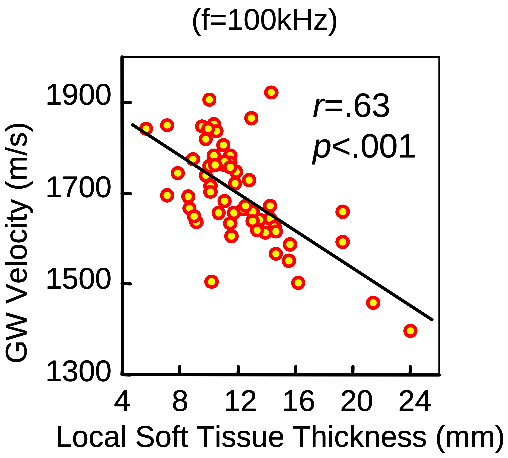

Fig. 6.16. Guided wave velocity v_2 (as determined using the selective spectral analysis and plate theory for the poor plate theory fit group) versus local soft tissue thickness for the radius in vivo.

The cortical thickness estimate h_e, as determined using the inversion scheme (plate model), was significantly higher than the actual cTh, and the correlation between h_e and cTh (good plate theory fit group) was slightly lower (but significant) than that of v_2. These observations were obviously caused by the compatibility issues between the simple plate model and the in vivo problem (as the bone has tubular shape and it is overlyed by a layer of soft tissue). However, the tube or bilayer models have not yet been tested with the inversion analysis of the in vivo data. Further work is needed to optimise the inversion scheme for in vivo measurements exploring the use of tube and bilayer models, but this was outside the scope of the current work. It may also be necessary to combine the two into a tubular bilayer model.

Chapter 7

Discussion

In this study we introduced an axial scanner device, operating at low ultrasonic frequencies (f = 50-350 kHz), and a method for measuring two ultrasonic wave modes (Wave 1 and Wave 2) simultaneously in cortical bone using this device. The measurement principle was verified with two-dimensional finite element simulations as well as with experimental measurements for bone phantoms. Wave 1 was shown to be the fast first arriving signal (FAS) and Wave 2 was consistent with the fundamental antisymmetric (or flexural) guided wave (A0). The effects of tubularity and overlying soft tissue were investigated theoretically and experimentally, and measurements were made on specific bone phantoms to illustrate the effect of anatomical bone shape. In addition, we reported guided wave results for human bone in vitro and in vivo - to our best knowledge, as the first group after Jansons et al [41] and Tatarinov et al [99].

The finite element simulations and the experimental results for plates were in excellent agreement with the theory of Lamb waves as well as with the previous finite difference simulation results by Bossy et al [11, 12] regarding the thickness effects of FAS. Wave 1, corresponding to FAS, was consistent with the lateral longitudinal wave if thickness-to-wavelength ratio was $e/\lambda >> 0.5$. When e/λ was close to 0.5, then a clear decrease in the velocity of Wave 1 was observed, and when $e/\lambda << 0.5$ Wave 1 was close to or consistent with the fundamental symmetric guided wave (S0). In addition, a slight increase in v_1 compared to its high-frequency saturation value (c_L) was observed at around e/λ = 0.7-1.0, which was as well in agreement with Bossy's results. According to our measurements for human bone, the cortical thickness varied in the range 2.5-6.5 mm in the tibia and 1.0-4.0 mm in the radius. When measuring Wave 1 (f = 250-300 kHz), these ranges correspond roughly to e/λ = 0.2-0.5 and e/λ = 0.1-0.3, respectively, indicating that Wave 1 is expected to be sensitive to cortical thickness in the tibia, and that in the radius the thickness sensitivity may be impaired due to plateau of S0. In comparison, the French prototype device (f = 1.0 MHz) corresponds respectively to e/λ = 0.6-1.6 and e/λ = 0.25-1.0, and Omnisense (f = 1.25 MHz) to e/λ > 0.8-2.0 and e/λ = 0.3-1.3. Thus, neither of these devices is expected to be sensitive to the cortical thickness of the tibia, but especially the French device may be sensitive to that of the radius.

Velocity v_2 of Wave 2 (f = 100 kHz), being consistent with A0, saturated to Rayleigh velocity c_R for $e/\lambda > 2$ (Figs 6.2, 6.4). For $e/\lambda < 2$, v_2 began to decrease slightly, and for $e/\lambda < 0.5$ strongly with decreasing e/λ. The cortical thicknesses measured in the tibia and radius correspond respectively to e/λ = 0.1-0.3 and e/λ = 0.2-0.5 when measuring

Wave 2 at f = 100 kHz (by chance similarly as with Wave 1). Thus, v_2 is expected to be highly sensitive to cortical thickness in the radius as well as in the tibia.

Measurements in vitro confirmed the thickness sensitivity of Wave 1 and Wave 2. The correlation between v_2 and cTh was strong and significant, partly confirming the consistency between Wave 2 and A0 guided wave. However, v_1 only yielded a modest correlation with cTh, which could partly be explained due to the S0 plateau effect at low e/λ. The inferiority of v_1 results could also be explained due to impaired coupling of Wave 1, as the low-frequency device is not optimised for measuring the Wave 1 alone. Transducers were orientated perpendicularly to the specimen, whereas properly tilted transducers would have concentrated more of the energy into the longitudinal wave. Also, the resolution of the data acquisition device (8 bits, 10 MHz) was limited and it was not possible to completely filter the digitising noise of the poorly coupled, low-intensity signals.

The main interest was in the investigation of the sensitivity of ultrasonic velocities to the cortical thickness. Therefore, the thickness was chosen (as an only material property) as the fitting parameter in the inversion scheme. In plates the plate theory inversion yielded exact thickness estimates h_e (10% precision) for plates thinner than 8 mm, which is considered as sufficient regarding the cortical thicknesses of human bones. However, when using the plate theory inversion in tubes, the estimate was exact only when the wall thickness e was low compared to the outer radius b of the tube ($e/b < 0.3$), but for e/b larger than that the error increased with increasing e/b. It was proposed that the difference between plate and tube models could explain this phenomenon, and successfully it was shown that using the tube model inversion, the thickness estimate h_e corresponded nicely (10% precision) to the actual tube wall thickness e, provided that $e/b < 0.8$ and $e < 8$ mm. This is indeed considered sufficient within the range of human bone cortical thicknesses.

The inversion for the human radius in vitro (mean $e/b = 0.4$) yielded the thickness estimate range h_e matching exactly to that of the actual cTh. However, the correlation between h_e and cTh was not higher than r=0.71 (p<0.001), and there was clear scattering in the points seen in Fig 6.11. This can obviously be explained due to the choice of constant tube radius b in the inversion model. This b was defined according to the mean radius of the radius bones, thus the variation of the actual radius clearly explains the scattering of the observed result. In addition to b, the elastic properties of the bone were assumed as constants, and this assumption affects scattering as well.

In addition, it was shown that v_1 and v_2 are dominated by the local rather than average thickness of anatomically shaped bone phantoms. This denotes that the placement and alignment of an ultrasonic probe on top of bone is critical in order to obtain reliable and reproducible results. However, when comparing the acoustic wavelengths between bone and PVC, the effective size of the anatomically shaped phantoms (made of PVC) matches to that of approximately 1.6 times greater bone. Therefore, as the diameter-to-wavelength ratio of actual human bones is smaller than in these experiments, the ultrasound velocities may more strongly be affected by the mean cortical thickness. This consideration can justify the use of the mean cortical thickness in the pQCT measurements of bone in vitro and in vivo. The mean thickness was much more precise than the local cortical thickness, which had to be determined using a slow manual analysis of the pQCT images.

The effect of the material properties (elastic modulus and density) on v_1 and v_2 was not considered in detail in the simulations or experimental measurements in phantoms. In theory, the material bulk velocities c_L and c_T are affected by Young's modulus E and density ρ, and Poisson's ratio ν according to Eqs. (3.1) and (3.2), where ν is defined by c_L and c_T as

$$\nu = \frac{1 - 2\left(\frac{c_T}{c_L}\right)^2}{2 - 2\left(\frac{c_T}{c_L}\right)^2} .$$

Biomechanical studies indicate that E is approximately proportional to ρ^n where estimates of n range in the literature from 2 to 3 in cortical bone. From Eq. 3.1 this implies that velocity should then be function of ρ^m where m should vary from 0.5 to1. This explains the positive correlations obtained between ultrasound velocities and the bone mineral density (BMD). As velocity v_1 saturates to c_L, and v_2 to $c_R \approx 0.9\ c_T$, this defines the relationships between v_1, v_2 and the elasticity and density via the bulk velocities of the material.

In general, the bulk velocities alone define the dispersion curves for a plate, and thus the inversion from the experimentally measured guided wave velocities is possible to the bulk velocities and further to elastic constants properties of the plate. This inversion approach has been successfully utilised, e.g., by Karim and Mal, Lefebvre et al and Gsell et al [44, 54, 34]. It is provided, however, that the thickness and density of the plate (or tube wall) are known. Considering the bone guided wave application, the thickness could, for instance, be measured using a simple pulse-echo measurement, in the contrary to the complicated guided wave inversion approach discussed in this study. As mentioned in Section 5.2.3, velocities of several genuine guided waves should be measured within a broad frequency range in order to successfully use the elastic modulus inversion. The thickness inversion approach was the most suitable for this application, as it also helped in solving the wave identification problems (due to low spatial resolution) together with the selective 2D-FFT method.

Remaining relevant questions that arise in the applicability of guided waves in the assessment of long bones are the effects of endosteal porosity, bone heterogeneity and anisotropy. It is known that anisotropy of cortical bone can be considered according to transversely isotropic or orthotropic symmetry [81]. In addition, the analytical guided wave models (plate and tube) can be expanded to anisotropic case, though a more general solution method must be used [87, 80, 34]. This must obviously be made next in the progress of bone guided waves research.

Endosteal porosity is also a critical issue, as it affects roughness of the inner cortical layer, and the theory of guided waves provides an ideal layer with smooth top and bottom surfaces. Clearly, the roughness scatters the partial ultrasonic waves, and consequently affects attenuation of the propagating guided wave. If the size of the scatterers is significantly smaller than the acoustic wavelength, then only the attenuation (without more complex effects) takes place and the guided wave is expected to propagate. As the size of the pores in endosteal bone is of the order or less than 1 mm, and the acoustic wavelength of the A0 guided wave is of the order of one or two centimetres (f = 100kHz), the condition between the pore size and wavelength is satisfied. However, as the frequency increases, the wavelength decreases. So, consequently the propagation of higher order guided waves may not be possible in the bone, especially in osteoporotic bone. The effect of surface roughness on guided waves has also been studied theoretically and experimentally by Lobkis and Chimenti [56, 57]. 3D simulations in bone [12] indicate that the increasing endosteal porosity decreases the velocity of the FAS. In addition, the experimental phantom measurements, made by Tatarinov et al [98], suggest that the velocity of flexural guided wave (i.e. A0) is decreased by the increased amount of endosteal porosity (f = 100 kHz). Thus, both Wave 1 and Wave 2 are expected to be affected by the porosity, in a manner that these low frequency ultrasonic waves in a way sense the effective thickness of the compact bone. As a conclusion, the low-frequency guided waves are therefore expected to be good indicators of the cortical thickness.

The in vivo results in a hundred-and-six pubertal girls were in an agreement with the in vitro results, suggesting correlations between the guided wave velocities (v_1, v_2) and bone properties (BMD, cTh). The correlations between the guided wave velocities and cortical BMD were, in general, as high as expected from the in vitro study. Velocity v_1 yielded slightly better correlation in vivo than in vitro, which may indicate that the overlying soft tissue improves the coupling of the longitudinal first arriving wave (Wave 1). Velocity v_2, in turn, was slightly lower than its in vitro counterpart. This clearly is the first sign to indicate the problems in the reliable identification of the fundamental flexural (or antisymmetric) guided wave (Wave 2) through the overlying soft tissue. However, the preliminary results comparing the small group of osteoporotic females with a normal healthy control group, in spite of the soft tissue effects, only the Wave 2 can significantly discriminate between osteoporotic and healthy bone. These data suggest that the guided waves may yield a clinically relevant bone assessment and thus justifies the need for more extensive in vivo measurements and further investigation and development of the method.

Further in vivo measurements were made for the tibia of sixty five and for the radius of a hundred and seven subjects. In the analysis of these measurements we, however, encountered serious difficulties in obtaining a good fit between Wave 2 and A0 plate mode. As a result, we found out that the difficulty in observing a clear A0 like Wave 2 increased with increasing on-site soft-tissue thickness. The classification based on the quality of plate theory fitting yielded the rejection of 1/3 to 2/3 of the subjects when choosing the sub-set of good fit data. This classification helped in obtaining the expected correlations between v_2 and bone quantities in the small good plate theory fit sub-sets. However, the only strong and clear (negative) correlation was obtained between v_2 and the soft tissue thickness in the sub-set classified as poor plate theory fit group. These findings, unfortunately, raise also the preliminary positive results into a doubtful light. In the preliminary phase Wave 2 was analysed using semi-automatic line fitting in (r,t) diagrams, and thus the human judgement of the proper fitting may have had a strong influence on the obtained v_2. Though being blind on the bone properties, the automatically determined v_1 was known when determining v_2. Later, different automatic analyses, based on filtering and line fitting in the distance-time plane or the spectral analysis, were developed to achieve more reliable determination of v_2. However, no expected correlations have, as yet, been obtained. The results do suggest that visual analysis of the (r,t) diagrams by a human observer may actually work better than the current automatic processing algorithms. This gives further confidence that there is valuable, though complicated, information present in the signals, and that further refinement of the signal analysis procedures is likely to bring improved results. The data also indicate that, for a human observer, knowledge of v_1 may improve the determination of v_2 and this suggests that automatic analysis based on the information from both waves is worth investigating.

These difficulties yielded the motivation for developing the fluid-solid bilayer model for explaining the effects of the overlying soft tissue layer. It is obvious to expect that the guided waves propagate, not in the bone or soft tissue alone, but in the whole bilayer system composed of bone and soft tissue. Therefore, it is highly possible that this bilayer model could explain the problem of in vivo guided wave measurement. In this model, the contribution of soft tissue is mostly related to the thickness of the soft overlayer (assuming that the sound speed in soft tissue can be approximated e.g. with that in water). This prediction is in close agreement with the experimentally obtained negative correlation between v_2 and soft tissue thickness. Therefore, the purpose is to use the soft tissue thickness a as the known input parameter in the inversion scheme and selective spectral analysis method, and this way to eliminate its effect by seeking for the contribution of bone thickness h alone (or any bone material parameter) to the experimentally measured bilayer velocities.

The limitations of the suggested solution approach to the soft tissue problem are tightly connected to those of the inversion scheme and selective two-dimensional spectral analysis method. The inversion was shown to work with plates, tubes and bones in vitro. As the thickness h_e was allowed to range over the whole spectrum of the results, it was shown that the inversion scheme works provided that a proper theory and input parameters are chosen. Therefore, the accuracy of this method relies on the choice of theoretical model and input parameters. Also, this means that satisfactory in vivo results cannot be obtained until the theory behind the guided wave propagation problem in vivo can be modelled and is known well enough. To this end the modelling of the effects of bone as tube, anisotropy, inhomogeneity and endosteal roughness are warranted. But more importantly, the effects of the overlying soft tissue and interior bone marrow should be addressed. Modelling the soft tissue or bone marrow as ideal elastic fluid may not, however, be sufficient, as the soft tissue and marrow are viscous (or visco-elastic) materials and may strongly affect the dispersion behaviour of guided waves. Previous studies, made regarding the effects of viscous tube core, viscous loading and visco-elastic bilayer [107, 108, 26, 71, 97], could be used as the starting point in these problems.

A strong limitation of the two-dimensional spectral analysis was the short spatial scanning length (typically 30 mm). The short scanning length was necessary as to be able to approximate that there is no significant variability in the bone properties within the scanning range. This, however, yielded flat spectral peaks and thus low resolution in discriminating different wave modes in the phase-velocity (or wavenumber) domain. As a result, joint peaks were formed if two wave modes were too close to each other (in many cases already, e.g., the phase velocity difference of 1000 m/s was too close). We tested the adverse effect of the short scanning length (results not shown here) by finite-element simulations, and a 200 mm scanning length, for instance, yielded an excellent peak resolution. The selective 2D-FFT method was developed in order to eliminate the effect of other wave modes and thus to improve the reliability of mode identification. The fast Fourier transform could, however, be replaced with some more efficient spectral analysis approach, such as the Prony method [108, 47] or matrix pencil method [40, 34]. Also, it could be worth of trying to try to extend the scanning length in order to improve the resolution. This, however, must be made by the cost of increasing variability of bone properties, which obviously may be adverse on the propagation of guided waves. But being able to measure guided waves over a longer range, then this could yield an average result reflecting more completely the properties (strength) of bone.

The ultimate question, which arises, is the clinical relevance of the bone assessment using the guided ultrasonic waves, a) in general and b) using the proposed measurement approach. Clinically it would be relevant to have methods which can discriminate between osteoporotic or fractured and a healthy bone. Also, it would be warranted to assess the early signs of bone deterioration and to predict the risk for bone fracture at an early phase, thus maximising the benefit of medication. It may be difficult to displace the dual energy x-ray absorptiometry, the “golden standard” of bone assessment, completely. However, in general ultrasound provides three advantages over the X-ray based methods. Ultrasound is believed to be tissue safe, as long as intensity levels are kept below well recognised maximum permissible levels, and the equipment can be built as small and easy-to-use devices with an economy price. But more importantly, ultrasonic velocity reflects the material elasticity as well as its density, whereas the X-ray absorption is only affected by the density. Therefore, the comparison between ultrasonic and X-ray methods should be made bearing in mind that these methods are expected to reflect quite different properties of bone. The density takes no account of the underlying hierarchical microstructure that defines the mechanical properties of bone. The density thus yields only a fraction of the information that is needed to define the strength of bone. For instance, disorganised bone, such as that found in Paget’s disease, may have normal density but dramatically reduced elastic modulus and is expected to be weak and fracture easily. However, X-ray absorption cannot predict this, provided that the density is close to the normal level. But the ultrasonic velocity gives a direct insight into the ratio between elasticity and density. Therefore, the ultrasonic velocity may reflect the bone strength more completely than X-ray attenuation, lacking, however, information of the absolute magnitude of the density.

The question of guided waves builds up on top of understanding of the behaviour of the ultrasonic waves in general, as the guided wave is composed of the conventional ultrasonic longitudinal and shear waves between two boundaries of a medium. As discussed in this Thesis, the velocities of the measured guided waves were strongly related to the thickness of the waveguide due to dispersion. It was also described that the guided wave is a bending vibration of the whole structure. The guided wave velocity can therefore reflect aspects of the average elasticity and density throughout the bone thickness, as well as the effective thickness itself. A broad-band guided wave measurement can yield a multivariable inversion problem, i.e. a set of guided wave velocities (v_e^i,f_i), which can with certain approximations be quite accurately inversed as different material properties of the medium in which they were measured from. Therefore, a single guided wave velocity, e.g. that we have referred to as v_2, can reflect only a fraction of the potential of guided waves. On the other hand it must be acknowledged that the possibility of measuring additional guided modes in bone has not yet been confirmed and hence the prospects for developing a successful inversion scheme for both geometric and material properties are not clear. Furthermore, even if a successful inversion scheme were possible allowing determination of elasticity, this would still only be a surrogate for bone strength rather than a direct measurement. It may be that optimal prediction of bone strength is to be obtained by combining a range of measurements including bone density, cortical thickness and elasticity.

Finally, however, theoretical considerations cannot, on their own, confirm the clinical applicability and value of a proposed new bone measurement method. This can only be made with in vivo measurements in large sample populations in comparison with the standard bone densitometry methods. A strength of this present study was its aim to collect such clinical evidence in the in vivo measurements. Measurements in girls confirmed the ability of guided waves to capture information on bone thickness in addition to bone density, in contrast to existing ultrasonic measurements of bone. Pilot data from a small number of older women suggested that guided waves may have an enhanced ability to detect osteoporosis. However, some difficulties were encountered in vivo due to the overlying soft tissue. In any future work, these difficulties should be addressed by extending the modelling work to include the modelling of bone as an anisotropic tube, and the soft tissue and bone marrow respectively as a viscous liquid layer and core. The large amounts of in vivo data that have been gathered already will be useful in any future work.

As, noted above, future work could thus include the development of an appropriate wave propagation model for a multilayer structure in order to better interpret the in vivo guided wave measurements in bone. In this model the bone should preferably be considered as an anisotropic tube, and the soft tissue and bone marrow respectively as a viscous liquid layer and core. In addition, further technical development of the measurement system is warranted. The speed of data acquisition should be increased, thereby enabling a better precision through increased signal averaging. Also, it would be warranted to move the recording position slightly sideways on top of the bone between the scans in order to seek for an optimal contact and signal response. All of these requirements could be achieved by an array probe in which the necessary transducer elements were built inside a single casing, and scanning could be performed electronically. Finally, the ultrasonic guided wave assessment of bone does not necessarily need to be limited in the transmission principle, but also the measurement of a specular reflection spectrum may be worth investigating. This approach has been successfully used for measuring the guided wave dispersion curves for composite laminates [6, 7], and it also provided an efficient implementation of an inversion scheme [44]. A similar approach, known as the Ultrasonic Critical angle Reflectometry (UCR), has been used for determining the pressure and shear wave speeds for bone [3, 63]. However, the reflection-based measurement of guided waves has not yet been reported for bone. This approach would be attractive as it provides a localised point measurement, and allows the simultaneous measurement of several guided wave modes.

As a conclusion, it was shown that the methods introduced in this Thesis provide useful information of bone phantoms and bone in vitro, and despite of the effects due to overlying soft tissues, also of bone in vivo. These results thereby indicate that the use of ultrasonic guided waves is a feasible and clinically useful assessment of cortical bone, providing advantages over the existing axial transmission techniques. In addition, this Thesis forms a firm basis for any future endeavours to improve the clinical performance of the guided wave bone assessment by further modelling work and technical development of the device and methods of analysis.

References

[1] D. Alleyne and P. Cawley, *A two-dimensional Fourier transform method for the measurement of propagating multimode signals*, J Acoust Soc Am **89** (1991) 1159-1168.

[2] Anonymous, *Consensus development conference: diagnosis, prophylaxis and treatment of osteoporosis*, Am J Med **94** (1993) 646-650.

[3] P. P. Antich, J. A. Anderson, R. B. Ashman, J. E. Dowdey, J. Gonzales, R. C. Murry, J. E. Zerwekh and C. Y. Pak, *Measurement of mechanical properties of bone material in vitro by ultrasound reflection: methodology and comparison with ultrasound transmission.*, J Bone Min Res **6** (1991) 417-426.

[4] C. Aristegui, M. J. S. Lowe and P. Cawley, *Guided waves in fluid-filled pipes surrounded by different fluids*, Ultrasonics **39** (2001) 367-375.

[5] R. B. Ashman, S. C. Cowin, W. C. van Buskirk and J. C. Rice, *A continuous wave technique for the measurement of the elastic properties of cortical bone*, J Biomechanics **17** (1984) 349-361.

[6] Y. Bar-Cohen, A. K. Mal and S. S. Lih, *NDE of composite materials using ultrasonic oblique insonification*, Materials Evaluation **51** (1993) 1285-1296.

[7] Y. Bar-Cohen, A. K. Mal, S. S. Lih and Z. Chang, *Composite materials stiffness determination and defects characterization using enhanced leaky Lamb wave dispersion data acquisition method*, Proc SPIE Int Soc Opt Eng **3586** (1999) 250-255.

[8] R. Baron, *Anatomy and ultrastructure of bone*, in M. J. Favus, ed., *Primer on the Metabolic Bone Diseases and Disorders of Mineral Metabolism* (Lippincott, Williams and Wilkins, Philadelphia, 1999, pp. 3-10).

[9] D. C. Bauer, C. C. Cluer, A. R. Pressman, T. M. Vogt, K. E. Ensrud, J. A. Cauley and et al, *Broadband ultrasonic attenuation (BUA) and the risk of fracture: a prospective study*, J Bone Miner Res **10** (1995) S175.

[10] E. Bossy, M. Talmant, M. Defontaine, F. Patat and P. Laugier, *Bidirectional axial transmission can improve accuracy and precision of ultrasonic velocity measurement in cortical bone: a validation on test materials*, J Acoust Soc Am **115** (2004) 2314-2324.

[11] E. Bossy, M. Talmant and P. Laugier, *Effect of bone cortical thickness on velocity measurements using ultrasonic axial transmission: a 2D simulation study*, J Acoust Soc Am **112** (2002) 297-307.

[12] E. Bossy, M. Talmant and P. Laugier, *Three-dimensional simulations of ultrasonic axial transmission velocity measurement on cortical bone models*, J Acoust Soc Am **115** (2004) 2314-2324.

[13] M. L. Bouxsein and P. Augat, *Biomechanics of bone*, in C. F. Njeh, D. Hans, T. Fuerst, C. C. Gluer and H. K. Genant, eds., *Quantitative Ultrasound: Assessment of Osteoporosis and Bone Status* (Martin Dunitz, London, 1999, pp. 21-46).

[14] J. A. Buckwalter, M. J. Glimcher, R. R. Cooper and R. Recker, *Bone biology. Part I: structure, blood supply, cells, matrix, and mineralization*, J Bone and Joint Surg **77-A** (1995) 1256-1275.

[15] J. A. Buckwalter, M. J. Glimcher, R. R. Cooper and R. Recker, *Bone biology. Part II: formation, form, modeling, remodeling, and regulation of cell function*, J Bone and Joint Surg **77-A** (1995) 1276-1289.

[16] E. Camus, M. Talmant, G. Berger and P. Laugier, *Analysis of the axial transmission technique for the assessment of skeletal status*, J Acoust Soc Am **108** (2000) 3058-65.

[17] M. Castaings and B. Hosten, *Lamb and SH waves generated and detected by air-coupled ultrasonic transducers in composite material plates*, NDT&E International **34** (2001) 249-58.

[18] J. D. N. Cheeke, X. Li and Z. Wang, *Observation of flexural Lamb waves (A0 mode) on water-filled cylindrical shells*, J Acoust Soc Am **104** (1998) 3678-3680.

[19] J. D. N. Cheeke, K. Shannon and Z. Wang, *Loading effects on A0 Lamb-like waves in full and partially filled thin-walled tubes*, Sensors and Actuators B **59** (1999) 180-3.

[20] D. E. Chimenti, *Guided waves in plates and their use in materials characterization*, Appl Mech Rev **50** (1997) 247-84.

[21] D. E. Chimenti and R. W. Martin, *Nondestructive evaluation of composite laminates by leaky Lamb waves*, Ultrasonics **29** (1991) 13.

[22] D. E. Chimenti and A. H. Nayfeh, *Leaky Lamb waves in fibrous composite laminates*, J Appl Phys **58** (1985) 4531-4538.

[23] C. C. Clüer, R. Eastell, D. M. Reid, D. Felsenberg, C. Roux, R. Barkmann, W. Timm, T. Blenk, G. Armbrecht, A. Stewart, J. Clowes, F. E. Thomasius and S. Kolta, *Association of five quantitative ultrasound devices and bone densitometry with osteoporotic vertebral fractures in a population-based sample: the OPUS study*, J Bone Miner Res **19** (2004) 782-792.

[24] G. Cohen, *Higher-Order Numerical Methods for Transient Wave Equations* (Springer-Verlag, Berlin, 2002).

[25] R. Eastell, *Pathogenesis of postmenopausal osteoporosis*, in M. J. Favus, ed., *Primer on the Metabolic Bone Diseases and Disorders of Mineral Metabolism* (Lippincott, Williams and Wilkins, Philadelphia, 1999, pp. 260-262).

[26] L. Elvira-Segura, *Acoustic wave dispersion in a cylindrical elastic tube filled with a viscous liquid*, Ultrasonics **37** (2000) 537-547.

[27] A. J. Foldes, A. Rimon, D. D. Keinan and M. M. Popovtzer, *Quantitative ultrasound of the tibia: a novel approach for assessment of bone status,* Bone **17** (1995) 363-7.

[28] M. L. Frost, G. M. Blake and I. Fogelman, *Quantitative ultrasound and bone mineral density are equally strongly associated with risk factors for osteoporosis,* J Bone Miner Res **16** (2001) 406-416.

[29] D. C. Gazis, *Three dimensional investigation of the propagation of waves in hollow circular cylinders I. Analytical foundation*, J Acoust Soc Am **31** (1958) 568-573.

[30] M. Gerlanc, D. Haddad, G. W. Hyatt, J. T. Langloh and P. St Hilaire, *Ultrasonic study of normal and fractured bone*, Clin Orthop (1975) 175-80.

[31] S. Goemaere, H. Zmierczak, I. Van Pottelberg and J. M. Kaufman, *Ability of peripheral bone assessments to predict areal bone mineral density at hip in community-dwelling elderly men*, J Clin Densitom **5** (2002) 219-228.

[32] K. F. Graff, *Wave Motion in Elastic Solids* (Dover, New York, 1991).

[33] S. Grondel, J. Assaad, C. Delebarre and E. Moulin, *Health monitoring of a composite wingbox structure*, Ultrasonics **42** (2004) 819-824.

[34] D. Gsell and J. Dual, *Non-destructive evaluation of elastic material properties in anisotropic circular cylindrical structures*, Accepted for publication in Ultrasonics (2004).

[35] D. Hans, P. Dargent-Molina, A. M. Schott, J. L. Sebert, C. Cormier, P. O. Kotzki, P. D. Delmas, J. M. Pouilles, G. Breart and P. J. Meunier, *Ultrasonographic heel measurements to predict hip fracture in elderly women: the EPIDOS prospective study*, Lancet **348** (1996) 511-514.

[36] D. Hans, S. K. Srivastav, C. Singal, R. Barkmann, C. F. Njeh, E. Kantorovich, C. C. Gluer and H. K. Genant, *Does combining the results from multiple bone sites measured by a new quantitative ultrasound device improve discrimination of hip fracture?*, J Bone Miner Res **14** (1999) 644-51.

[37] W. C. Hayes, *Biomechanics of cortical and trabecular bone: implications for assessment of fracture risk*, in V. C. Mow and W. C. Hayes, eds., *Basic Orthopaedic Biomechanics* (Raven Press, New York, 1991, pp. 93-142).

[38] R. P. Heaney, L. V. Avioli, C. H. I. Chesnut, J. Lappe, R. R. Recker and G. H. Brandenburger, *Ultrasound velocity through bone predicts incident vertebral deformity*, J Bone Miner Res **10** (1995) 341-345.

[39] B. K. Hoffmeister, S. R. Smith, S. M. Handley and J. Y. Rho, *Anisotropy of Young's modulus of human tibial cortical bone,* Med Biol Eng Comput **38** (2000) 333-8.

[40] Y. Hua and T. K. Sarkar, *Matrix pencil method for estimating parameters of exponentially damped/undamped sinusoids in noise,* IEEE Transactions on Acoustics, Speech, and Signal Processing **38** (1990) 814-824.

[41] H. Jansons, A. Tatarinov, V. Dzenis and A. Kregers, *Constructional peculiarities of the human tibia defined by reference to ultrasound measurement data*, Biomaterials **5** (1984) 221-6.

[42] P. Kannus, S. Niemi, J. Parkkari, M. Palvanen, I. Vuori and M. Järvinen, *Hip fractures in Finland between 1970 and 1997 and predictions for the future*, Lancet **353** (1999) 802-805.

[43] P. Kannus, J. Parkkari and S. Niemi, *Prevention of hip fracture in elderly people with use of a hip protector*, N Eng J Med **343** (2000) 1506-1513.

[44] M. R. Karim, A. K. Mal and Y. Bar-Cohen, *Inversion of leaky Lamb wave data by simplex algorithm*, J Acoust Soc Am **88** (1990) 482-91.

[45] K. T. Khaw, J. Reeve, R. Luben, S. Bingham, A. Welch, N. Warenham, S. Oakes and N. Day, *Prediction of total and hip fracture risk in men and women by quantitative ultrasound of calcaneus: EPIC-Norfolk prospective population study*, Lancet **363** (2004) 197-202.

[46] G. L. Klein, *Nutritional rickets and osteomalacia*, in M. J. Favus, ed., *Primer on the Metabolic Bone Diseases and Disorders of Mineral Metabolism* (Lippincott, Williams and Wilkins, Philadelphia, 1999, pp. 315-318.).

[47] M. Kley, C. Valle, L. J. Jacobs, L. Qu and J. Jarzynski, *Development of dispersion curves for two-layered cylinders using laser ultrasonics*, J Acoust Soc Am **106** (1999) 582-588.

[48] K. M. Knapp, G. M. Blake, T. D. Spector and I. Fogelman, *Multisite quantitative ultrasound: precision, age- and menopause-related changes, fracture discrimination, and T-score equivalence with dual-energy X-ray absorptiometry*, Osteoporosis Int **12** (2001) 456-464.

[49] R. Lakes, H. S. Yoon and J. L. Katz, *Ultrasonic waves propagation and attenuation in wet bone,* J Biomed Eng **8** (1986) 143-148.

[50] H. Lamb, *On waves in an elastic plate*, Proc Royal Soc **A93** (1917) 114-128.

[51] P. Laugier, *The basic physics of ultrasound*, in C. F. Njeh, D. Hans, T. Fuerst, C. C. Gluer and H. K. Genant, eds., *Quantiative ultrasound assessment of osteoporosis and bone status* (Martin Dunitz, London, 1999, pp. 47-66).

[52] K. I. Lee and S. W. Yoon, *Feasibility of bone assessment with leaky Lamb waves in bone phantoms and a bovine tibia*, J Acoust Soc Am **115** (2004) 3210-3217.

[53] S. C. Lee, B. S. Coan and M. L. Bouxsein, *Tibial ultrasound velocity measured in situ predicts the material properties of tibial cortical bone*, Bone **21** (1997) 119-25.

[54] F. Lefebvre, Y. Deblock, P. Campistron, D. Ahite and J. J. Fabre, *Development of a new ultrasonic technique for bone and biomaterials in vitro characterization*, J Biomed Mater Res **63** (2002) 441-6.

[55] R. Lindsay and F. Cosman, *Prevention of osteoporosis*, in M. J. Favus, ed., *Primer on the Metabolic Bone Diseases and Disorders of Mineral Metabolism* (Lippincott, Williams and Wilkins, Philadelphia, 1999, pp. 264-270).

[56] O. I. Lobkis and D. E. Chimenti, *Elastic guided waves in plates with surface roughness. I. Model calculation*, J Acoust Soc Am **102** (1997) 143-149.

[57] O. I. Lobkis and D. E. Chimenti, *Elastic guided waves in plates with surface roughness. II. Experiments*, J Acoust Soc Am **102** (1997) 150-159.

[58] R. Long, M. J. S. Lowe and P. Cawley, *Axisymmetric modes that propagate in buried iron water pipes*, in D. O. Thompson and D. E. Chimenti, eds., *Review of Progress in Quantitative Nondestructive Evaluation: Vol. 22* (American Institute of Physics, Plenum Press, New York, 2003, pp. 1201-1208).

[59] M. J. S. Lowe, *Matrix techniques for modeling ultrasonic waves in multilayered media*, IEEE Transactions on Ultrasonics, Ferroelectrics, and Frequency Control **42** (1995) 525-542.

[60] G. Lowet and G. Van der Perre, *Ultrasound velocity measurement in long bones: measurement method and simulation of ultrasound wave propagation*, J Biomech **29** (1996) 1255-62.

[61] R. B. Martin, D. B. Burr and N. A. Sharkey, *Skeletal Tissue Mechanics* (Springer-Verlag, New York, 1998).

[62] I. McCarthy, A. Goodship, R. Herzog, V. Oganov, E. Stussi and M. Vahlensieck, *Investigation of bone changes in microgravity during long and short duration space flight: comparison of techniques*, Eur J Clin Invest **30** (2000) 1044-1054.

[63] S. S. Mehta and P. P. Antich, *Measurement of shear-wave velocity by ultrasound critical-angle reflectometry (UCR)*, Ultrasound Med Biol **23** (1997) 1123-1126.

[64] W. Moher and P. Holler, *On inspectionof thin walled tubes for transverse and longitudinal flaws by guided ultrasonic waves*, Transactions on Sonics and Ultrasonics **SU-23** (1976) 369-374.

[65] A. J. Mortimer, *Physical characteristics of ultrasound*, in M. H. Repacholi and D. A. Benwell, eds., *Essentials of medical ultrasound: a practical introduction to the principles, techniques and biomedical applications* (Humana, Clifton, 1982, pp. 1-34).

[66] F. Moser, L. J. Jacobs and J. Qu, *Modeling elastic wave propagation in waveguides with the finite element method*, NDT & E International **32** (1999) 225-234.

[67] J. M. Muggleton, M. J. Brennan and R. J. Pinnington, *Wavenumber prediction of waves in buried pipes for water leak detection*, Journal of Sound and Vibration **249** (2002) 939-954.

[68] G. T. Mundy, *Bone remodelling*, in M. J. Favus, ed., *Primer on the Metabolic Bone Diseases and Disorders of Mineral Metabolism* (Lippincott, Williams and Wilkins, Philadelphia, 1999, pp. 30-38).

[69] A. H. Nayfeh, *The general problem of elastic wave propagation in multilayered anisotropic media*, J Acoust Soc Am **89** (1991) 1521-1531.

[70] A. H. Nayfeh and D. E. Chimenti, *Ultrasonic wave reflection from liquid-coupled orthotropic plates with application to fibrous composites*, J Appl Mech **55** (1988) 863-870.

[71] A. H. Nayfeh and P. B. Nagy, *Excess attenuation of leaky Lamb waves due to viscous fluid loading*, J Acoust Soc Am **101** (1997) 2649-2658.

[72] P. H. F. Nicholson, P. Moilanen, T. Kärkkäinen, J. Timonen and S. Cheng, *Guided ultrasonic waves in long bones: modelling, experiment and in vivo application*, Physiol Meas **23** (2002) 755-68.

[73] C. F. Njeh, X. G. Cheng, J. M. Elliot and P. J. Meunier, *Bone, bone diseases and bone quality*, in C. F. Njeh, D. Hans, T. Fuerst, C. C. Gluer and H. K. Genant, eds., *Quantitative Ultrasound: Assessment of Osteoporosis and Bone Status* (Martin Dunitz, London, 1999, pp. 1-20).

[74] C. F. Njeh, D. Hans, C. Wu, E. Kantorovich, M. Sister, T. Fuerst and H. K. Genant, *An in vitro investigation of the dependence on sample thickness of the speed of sound along the specimen*, Med Eng Phys **21** (1999) 651-9.

[75] C. F. Njeh, A. Richards, C. M. Boivin, D. Hans, T. Fuerst and H. V. Genant, *Factors influencing the speed of sound through the proximal phalanges*, J Clin Densitom **2** (1999) 241-249.

[76] I. Nurmi, A. Narinen, P. Luthje and S. Tanninen, *Cost analysis of hip fracture treatment among the elderly for the public health services: a 1-year prospective study in 106 consecutive patients*, Arch Orthop Trauma Surg **123** (2003) 551-554.

[77] B. R. Olsen, *Bone morphogenesis and embryonic development*, in M. J. Favus, ed., *Primer on the Metabolic Bone Diseases and Disorders of Mineral Metabolism* (Lippincott, Williams and Wilkins, Philadelphia, 1999, pp. 11-14).

[78] V. S. Oranov, A. S. Rakhmanov, B. V. Morukov, A. Ianson Kh and A. M. Tatarinov, *[Bone examination by noninvasive methods during prolonged hypokinesia]*, Kosm Biol Aviakosm Med **22** (1988) 30-3.

[79] A. M. Parfitt, *Age-related structural changes in trabecular and cortical bone: cellular mechanisms and biochemical consequences*, Calsif Tissue Int **36** (1984) S123-S128.

[80] B. N. Pavlakovic, *Leaky guided ultrasonic waves in NDT*, Ph.D. Thesis, *Imperial College of Science, Technology, and Medicine* (University of London, London, 1998).

[81] M. Pithioux, P. Lasaygues and P. Chabrand, *An alternative ultrasonic method for measuring the elastic properties of cortical bone*, Journal of Biomechanics **32** (2002) 961-968.

[82] S. M. F. Pluijm, W. C. Graafmans, L. M. Bouter and P. Lips, *Ultrasound measurements for the prediction of osteoporotic fractures in elderly people*, Osteoporos Int **9** (1999) 550-556.

[83] S. Prevrhal, T. Fuerst, B. Fan, C. Njeh, D. Hans, M. Uffmann, S. Srivastav and H. K. Genant, *Quantitative ultrasound of the tibia depends on both cortical density and thickness*, Osteoporos Int **12** (2001) 28-34.

[84] F. Rauch and F. H. Glorieux, *Osteogenesis imperfecta*, Lancet **363** (2004) 1377-1385.

[85] J. Y. Rho, *An ultrasonic method for measuring the elastic properties of human tibial cortical and cancellous bone*, Ultrasonics **34** (1996) 777-783.

[86] J. Y. Rho, L. Kuhn-Spearing and P. Zioupos, *Mechanical properties and the hierarchical structure of bone.*, Med Eng Phys **20** (1998) 92-102.

[87] J. L. Rose, *Ultrasonic waves in solid media* (Cambridge University Press, Cambridge, 1999).

[88] C. R. Rosen, *Anatomy, physiology and disease*, in C. M. Langton and C. F. Njeh, eds., *The Physical Measurement of Bone* (Institute of Physics Publishing, Bristol, UK, 2004, pp. 3-34).

[89] L. Rosenthal, J. Caminis and A. Tenenhouse, *Correlation of ultrasound velocity in the tibial cortex, calcaneal ultrasonography, and bone mineral densitometry of spine and femur*, Calcif Tissue Int **58** (1996) 415-418.

[90] C. T. Rubin and J. Rubin, *Biomechanics of bone*, in M. J. Favus, ed., *Primer on the Metabolic Bone Diseases and Disorders of Mineral Metabolism* (Lippincott, Williams and Wilkins, Philadelphia, 1999, pp. 39-42).

[91] S. Sakata, R. Barkmann, E. M. Lochmüller, M. Heller and C. C. Clüer, *Assessing bone status beyond BMD: evaluation of bone geometry and porosity by quantitative ultrasound of human finger phalanges*, J Bone Miner Res **19** (2004) 924-930.

[92] J. Saulgozis, I. Pontaga, G. Lowet and G. Van der Perre, *The effect of fracture and fracture fixation on ultrasonic velocity and attenuation*, Physiol Meas **17** (1996) 201-11.

[93] R. Seifried, L. J. Jacobs and J. Qu, *Propagation of guided waves in adhesive bonded components*, NDT & E International **35** (2002) 317-328.

[94] I. M. Siegel, G. T. Anast and T. Fields, *The determination of fracture healing by measurement of sound velocity across the fracture site*, Surg Gynecol Obstet **107** (1958) 327-332.

[95] H. Sievanen, S. Cheng, S. Ollikainen and K. Uusi-Rasi, *Ultrasound velocity and cortical bone characteristics in vivo*, Osteoporos Int **12** (2001) 399-405.

[96] M. G. Silk and K. F. Bainton, *The propagation metal tubing of ultrasonic wave mode equivalent to Lamb waves*, Ultrasonics **17** (1979) 11-19.

[97] F. Simonetti, *Lamb wave propagation in elastic plates coated with viscoelastic medium*, J Acoust Soc Am **115** (2004) 2041-2053.

[98] A. Tatarinov and A. Sarvazyan, *Dual-frequency method for ultrasonic assessment of bones: model study*, in D. Cassereau, ed., *5th World Congress on Ultrasonics*, Paris, 2003, 895-898).

[99] A. M. Tatarinov, S. L. Dubonos, A. Ianson Kh, V. S. Oganov, V. V. Dzenis and A. S. Rakhmanov, *[Ultrasonic diagnosis of the changes in human tibia during 370-day antiorthostatic hypokinesia]*, Kosm Biol Aviakosm Med **24** (1990) 29-31.

[100] J. Töyräs, *Mechano-acoustic characterization of articular cartilage and trabecular bone*, Ph.D. Thesis, *Department of Clinical Physiology and Nuclear Medicine* (Kuopio University Hospital and University of Kuopio, Kuopio, 2001).

[101] W. C. Van Buskirk and S. C. Cowin, *Ultrasonic measurement of the orthotropic elastic constants of bovine femoral bone*, J Biomech Eng **103** (1981) 67-72.

[102] G. Van der Perre and G. Lowet, *In vivo assessment of bone mechanical properties by vibration and ultrasonic wave propagation analysis*, Bone **18 Suppl 1** (1996) 29S-35S.

[103] R. D. Wasnich, *Epidemiology of osteoporosis*, in M. J. Favus, ed., *Primer on the Metabolic Bone Diseases and Disorders of Mineral Metabolism* (Lippincott, Williams and Wilkins, Philadelphia, 1999, pp. 257-259).

[104] P. N. T. Wells, *Biomedical Ultrasonics* (Academic Press, London, 1977).

[105] P. M. Whyte, *Osteogenesis imperfecta*, in M. J. Favus, ed., *Primer on the Metabolic Bone Diseases and Disorders of Mineral Metabolism* (Lippincott, Williams and Wilkins, Philadelphia, 1999, pp. 257-259).

[106] I. A. Viktorov, *Rayleigh and Lamb Waves* (Plenum Press, New York, 1967).

[107] J. Vollmann and J. Dual, *High-resolution analysis of the complex wave spectrum in a cylindrical shell containing a viscoelastic medium. Part I. Theory and numerical results*, J Acoust Soc Am **102** (1997) 896-908.

[108] J. Vollmann and J. Dual, *High-resolution analysis of the complex wave spectrum in a cylindrical shell containing a viscoelastic medium. Part II. Experimental results versus theory*, J Acoust Soc Am **102** (1997) 909-20.

[109] D. C. Worlton, *Experimental confirmation of Lamb waves at megacycle frequencies*, J Appl Phys **32** (1961) 967-971.

[110] D. C. Worlton, *Ultrasonic testing with Lamb waves*, Non-Destructive Testing **15** (1957) 218-222.

[111] C. L. Yapura and V. K. Kinra, *Guided waves in a fluid-solid bilayer*, Wave Motion **21** (1995) 35-46.

[112] J. J. R. Zemmanek, *An experimental and theoretical investigation of elastic wave propagation in a cylinder*, J Acoust Soc Am **52** (1972) 265-283.

[113] O. C. Zienkiewicz, *The Finite Element Method - 3rd Edition* (McGraw Hill, London, 1977).